Available online at www.sciencedirect.com

ScienceDirect

Advances in Space Research 73 (2024) 5783–5805

ADVANCES IN SPACE RESEARCH
(a COSPAR publication)

www.elsevier.com/locate/asr

GRACE Follow-On accelerometer data recovery by high-precision environment modelling

Moritz Huckfeldt [a,*], Florian Wöske [a], Benny Rievers [a,b], Meike List [c,d]

[a] *Center of Applied Space Technology and Microgravity (ZARM), University of Bremen, Am Fallturm 2, 28359 Bremen, Germany*
[b] *Gauss-Olber Space Technology Transfer Center Bremen, Bibliothekstraße 1, 28359 Bremen, Germany*
[c] *German Aerospace Center (DLR), Institute for Satellite Geodesy and Inertial Sensing, Callinstr. 30b, 30167 Hannover, Germany*
[d] *University of Bremen, Bibliothekstraße 1, 28359 Bremen, Germany*

Received 19 July 2023; received in revised form 22 March 2024; accepted 26 March 2024
Available online 1 April 2024

Abstract

The Gravity Recovery and Climate Experiment Follow-On (GRACE-FO) satellites are equipped with high-precision three-axis accelerometers to measure all non-gravitational accelerations acting on the satellites. Precise knowledge of these perturbations is a major prerequisite for successful Gravity Field Recovery (GFR). Unfortunately, after only one month in orbit the accelerometer on one of the two satellites produced decreasingly accurate measurements. Due to this, the GRACE-D accelerometer data has to be replaced by artificial data for the use in the GFR process. In most existing approaches, which are called transplants, this data is constructed from GRACE-C measurements.

We are developing a GRACE-D accelerometer product that relies mainly on modelled acceleration data instead of a full transplant. By using physical models to generate acceleration data, we are able to better understand the accelerometer signal and its characteristics, which is beneficial for subsequent processes involving accelerometer data. We present the evaluation of our modelled data in terms of comparison to the official Science Data System (SDS) accelerometer data. For the first GRACE-FO satellite real accelerometer is used as a reference, but for the second satellite the main comparisons are done with respect to the ACH1B transplant data product. To get information about environmental changes and long-term effects data sets covering one year and nearly the whole mission duration are presented. In terms of gravity field solutions the performance of purely modelled accelerometer data for GRACE-D and a minimalistic transplant approach of estimated density values is compared to transplant products of other processing centres for the year 2019 as well as one month of 2023. Through this, the modelled solution can act as a cross-reference to the transplant, contributing to an improved implementation of the external perturbation characteristics and the influence of higher solar activity on our models and the subsequent gravity field solutions can be determined.

Comparison of the artificial acceleration data to the real ACT1B data for GRACE-C showed that models related to the atmospheric drag are the limiting factors in our high-precision environment modelling approach. Nevertheless, it was still possible to generate monthly gravity field solutions with a combination of ACT1B data for GRACE-C and artificial data for GRACE-D that showed hydrological signals. Application of the transplant that substitutes the limiting modelled thermospheric density with estimated values obtained at GRACE-C positions reduces the residuals between artificial and real acceleration data significantly.

Estimation of gravity fields showed that the improvements due to the transplant directly transfer into the gravity field solutions. Our minimalistic and physically motivated transplant is shown to be a valuable alternative to the transplant data from TUG and JPL. The GROOPS software is utilized to generate monthly gravity field solution to guarantee comparability of the presented solutions for the geodesy community. The presented results not only show the quality of our transplant product but also enabled us to identify potential areas of improvement in the data generation process and our in–house gravity field recovery tool.

* Corresponding author.
E-mail addresses: moritz.huckfeldt@zarm.uni-bremen.de (M. Huckfeldt), florian.woeske@zarm.uni-bremen.de (F. Wöske), benny.rievers@zarm.uni-bremen.de (B. Rievers), meike.list@dlr.de (M. List).

https://doi.org/10.1016/j.asr.2024.03.068
0273-1177/

The ZARM GRACE-D transplant product, all radiation accelerations and estimated density is available for download at: https://www.zarm.uni-bremen.de/zarm_daten/.

Keywords: Geodesy; Gravity field; Accelerometer; Environment modelling; Transplant

1. Introduction

For the Gravity Recovery and Climate Experiment (GRACE) mission (Tapley et al., 2004), the accelerometer data is one of the main observations that enables researchers to continuously map the gravitational field of the Earth. The accelerometer on the second GRACE Follow-On (GRACE-FO) (Landerer et al., 2020) satellite, GRACE-D, produces data of reduced quality since about one month after the launch on 22 May 2018. Due to this, the accelerometer data of GRACE-D is replaced by artificial data based on GRACE-C acceleration observation and GRACE-D thruster information (Landerer et al., 2020; Harvey et al., 2022). A so called transplant procedure was developed in the last months of the GRACE mission to account for missing data from the accelerometer on GRACE-B, which was switched off to conserve power (Bandikova et al., 2019). Since then, the transplant process has been adapted for GRACE-FO at JPL (Landerer et al., 2020), as well as at the Graz Technical University (TUG), to generate more precise GRACE-D data (Behzadpour et al., 2021). This procedure is possible, because the two satellites fly on approximately the same orbit and pass the same position only 20 s to 30 s apart.

In this work, we describe the development of a procedure to generate artificial GRACE-D data, that is mostly independent of GRACE-C data, as an alternative transplant approach. Due to a slightly different attitude of the satellites, the non-gravitational-surface forces acting on the satellites are not the same for both. Hence just applying a time shift and attitude transformation to the accelerometer data does not provide the best accuracy. Using high fidelity models, it is possible to incorporate the strong dependence of the non-gravitational accelerations with respect to the exact attitude. We evaluate our approaches in two ways. First, we compare our artificial data to the official Science Data System (SDS) accelerometer data. This can be done for GRACE-C to real accelerometer data for nearly the complete mission duration. Comparison to real accelerometer data for GRACE-D is not possible due to the early corruption of accelerometer data and out gassing in the early mission days. The comparison of the data products gives information about which models are best suited for the GRACE-D data generation as well as the limits of the modelling approach. Second, we use the generated data for the gravity field processing and investigate the effects on the gravity field solutions. To increase the data quality past the limitations of atmospheric models, a minimalistic transplant approach is developed in which a density is estimated at GRACE-C positions and transplanted in time to GRACE-D positions. This procedure includes calibration of the accelerometer data with external parameters obtained from Precise Orbit Determination (POD) to avoid fitting modelling errors in the estimation. We aim to perform the transplant in the most physically accurate way possible, which potentially allows us to investigate the effect of all non-gravitational perturbations separately or combined on the performance of gravity field solutions. The performance of multiple transplant variations compared to the transplant procedures of JPL (McCullough et al., 2022) and TUG (Behzadpour et al., 2021) is done with the GROOPS software tool from TUG (Mayer-Gürr et al., 2021). For completeness of the description of our procedure, the processing of Level 1A to 1B data is explained. This is done in–house to get the accelerations induced by thruster firings for both satellites for the generation of thruster-free accelerometer data which allows us to do the comparison of artificial and official data as precise as possible.

2. Accelerometer data processing

For the processing scheme in this section we follow the procedure as previously implemented by Behzadpour et al. (2021) and defined in Wu et al. (2006) (see illustration in Fig. 2). Detailed information about the used data products can be found in Wen et al. (2019).

Each GFO satellite contains a three-axis electrostatic accelerometer produced by the Office National d'Études et de Recherches Aérospatiales (ONERA) (Christophe et al., 2015). The accelerometer is mounted at the centre

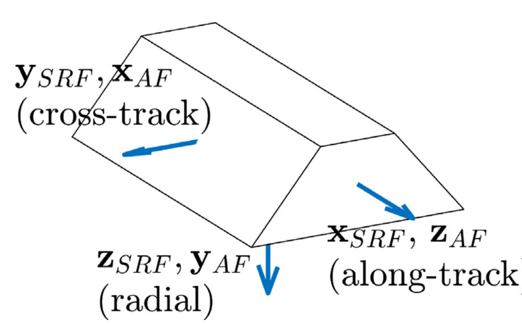

Fig. 1. The satellite-body fixed frames in relation to the satellite body: science-reference frame (SRF), accelerometer frame (AF). Illustration based on Harvey et al. (2022).

of mass (CoM) of the satellite and provides information about the linear and angular acceleration. The linear accelerations are measured with an accuracy better than 0.1 nm/$(s^2\sqrt{Hz})$ in the z- and x-axes and 1 nm/$(s^2\sqrt{Hz})$ in the y-axis of the accelerometer frame (AF) (Kornfeld et al., 2019), which is defined at the same position as the satellite's body frame as depicted in Fig. 1 (Harvey et al., 2022).

Due to the stringent satellite attitude control, the spacecraft's body axes are mainly aligned with the orbital frame: along-track, cross-track and radial. Hence, they are often referred to by the orbital frame terms in the GRACE community. Nevertheless, they differ slightly of around $\pm 1^{\circ}$.

Here, the processing from ACT1A to ACT1B data as implemented for our application is described. The ACT1A to ACT1B processing is done in–house to generate thruster-free data to use as a reference for our simulated acceleration data as well as thruster-only data to generate full accelerometer data from the simulated acceleration that can be used in GFR. The extraction of the accelerations induced by thruster firings is done from 10 Hz instead of 1 Hz data because they are visible in the accelerometer data as sharp spikes in the ACT1A product. In the ACT1B data the thruster spikes are smeared over a duration of more than a minute by the CRN low-pass filter due to their asymmetric shape (Bandikova et al., 2019) and extraction would not be possible without large data gaps.

2.1. Processing

The ACT1A to ACT1B processing is based on the ACC compression procedure given by Wu et al. (2006) and extended by the thruster-firing elimination as pictured in Fig. 2. Cutting the thruster response from the accelerometer data was done out of convenience as opposed to developing our own thruster model. With the recent publication of the ACX data product there is also a dedicated thruster data product AC0 available to obtain 1 Hz thruster accelerations, which is not incorporated in our procedure, yet.

The thrust-only data set is generated in the following steps. First, the GPS time-tag correction of the ACT1A data including resampling to integer-multiples of 0.1 s time-steps is done, so that all used data sets are given with respect to the same epoch. Then, the thruster firings are cut from the acceleration data with a certain margin before and after the firing, whose time stamp is given by the THR1B data. The determination of the margin length cut from the data set is explained in the next paragraph. Next, the gap is linearly interpolated to generate thrust-free acceleration data ($ACT1A_{woTHR}$). The final step is the subtraction of the thruster-free from the full acceleration to generate the thruster-only data set ($ACT1A_{THR}$):

$$ACT1A_{THR} = ACT1A - ACT1A_{woTHR}. \tag{1}$$

The three data sets in Eq. 1 have a sampling rate of 10 Hz and are put in the CRN filter to generate Level 1B data sets with 1 Hz sampling. After filtering the thruster-only data set is added to our modelled acceleration data for use in gravity field recovery and comparison with SDS ACT1B data as described in Section 3.5. For the ACH1B data product the thruster elimination is based on the $ACT1B_{THR}$ data for GRACE-D. The thrust-only data is subtracted from the ACH1B data to get thrust-free data sets:

$$ACH1B_{woTHR} = ACH1B - ACT1B_{THR}. \tag{2}$$

Each thruster pair is turned on for varying durations and induces different accelerations in the three SRF axes. Therefore, one year of GFO data was used to determine the length of the induced thruster spikes in the accelerometer data for each thruster pair and firing time. Linear interpolation is used to determine the margin for arbitrary firing durations based on the data used in the analysis. Fig. 3 shows the maximum length of a thruster spike depending on the thruster activation time for thruster pairs in roll, pitch and yaw directions for both satellites. Each data point represents a particular activation duration with no information about the number of activations of this duration. It is not distinguished between positive and negative directed thruster pairs. It can be seen that the length of the thruster spikes at GRACE-D is shorter for the same thruster activation time at GRACE-C. The data labelled *operational margin* in Fig. 3 corresponds to the maximum length of the thruster spikes and defines the length of data that is cut from the accelerometer data. The operational margin is chosen according to the GRACE-C thruster

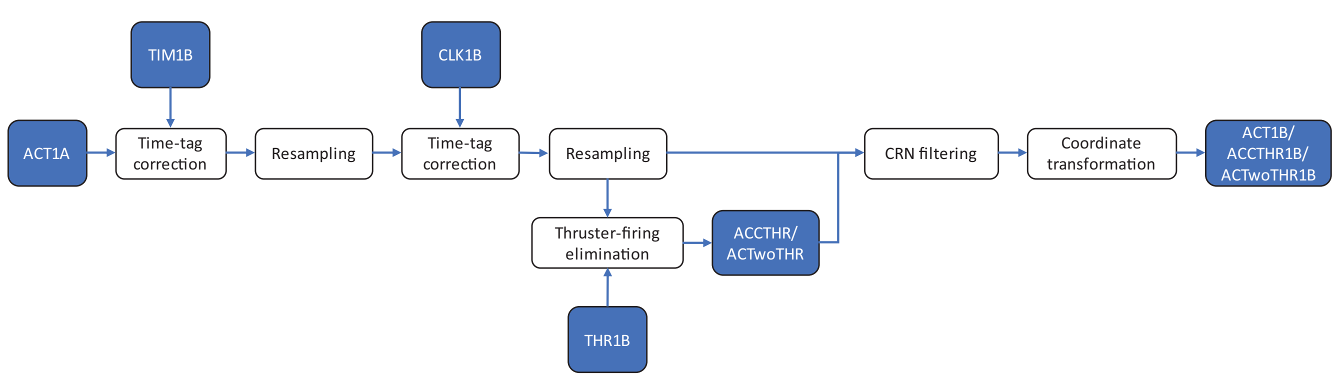

Fig. 2. Procedure, based on (Wu et al., 2006), to compress linear accelerations in ACT1A to ACT1B extended to eliminate and isolate accelerations from thruster firings. Figure based on Behzadpour et al. (2021).

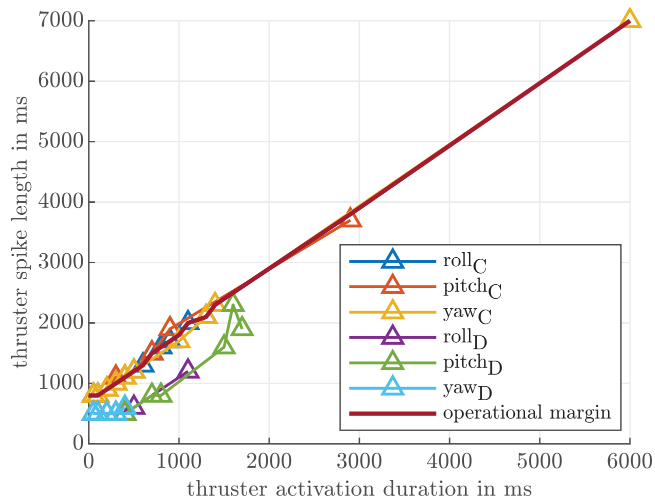

Fig. 3. The duration of thruster spikes in the accelerometer data depending on the activation duration and the firing direction of the thruster pair. Data is based on thruster firings that occur over 365 days for both GFO satellites (subscripts C and D) and used to determine the operational margin to eliminate thruster spikes from accelerometer data. Linear interpolation can be used to determine the margin for arbitrary activation lengths.

spike lengths and applied for both satellites. This value describes the time-span that has to be cut after the thruster activation timestamp given in the THR1B data and is clearly depending on the activation duration. The margin that has to be cut before the thruster activation timestamp is constant for all thruster pairs and activation times and was also determined in this analysis to 500 ms.

2.2. Validation

To validate the ACT1A to ACT1B processing we compare the in–house generated ACT1B (ZARM ACT1B) to the official SDS ACT1B. The comparison of both data sets for GRACE-C for a period of 6 h on 2 June 2019 is shown in Fig. 4 as time series and amplitude spectral density. The maximum deviations are in the 10^{-5}nm/s^2 range, which is several orders of magnitude smaller than the precision of the accelerometer (Kornfeld et al., 2019). This demonstrates the quality of our implementation. From these results, we can also derive that the other two generated data sets ($ACT1B_{woTHR}, ACH1B_{woTHR}, ACTC1B_{THR}$) have the same accuracy and can safely be used in future processes.

3. High-precision environment modelling

High-precision environment modelling is based on numeric simulation of the space-environment and satellite-induced perturbations with the eXtended Hybrid simulation Platform for Space systems (XHPS). The XHPS is a multi-satellite simulation tool with advanced calculation schemes to achieve high fidelity and fast computation. It is developed at the Center of Applied Space Technology and Microgravity (ZARM) and the German Aerospace Center (DLR).

For a detailed description of all considered perturbations the reader is referred to Wöske et al. (2019). Here, only a brief overview and description of the GFO specific setup is given. A summary of all considered models and

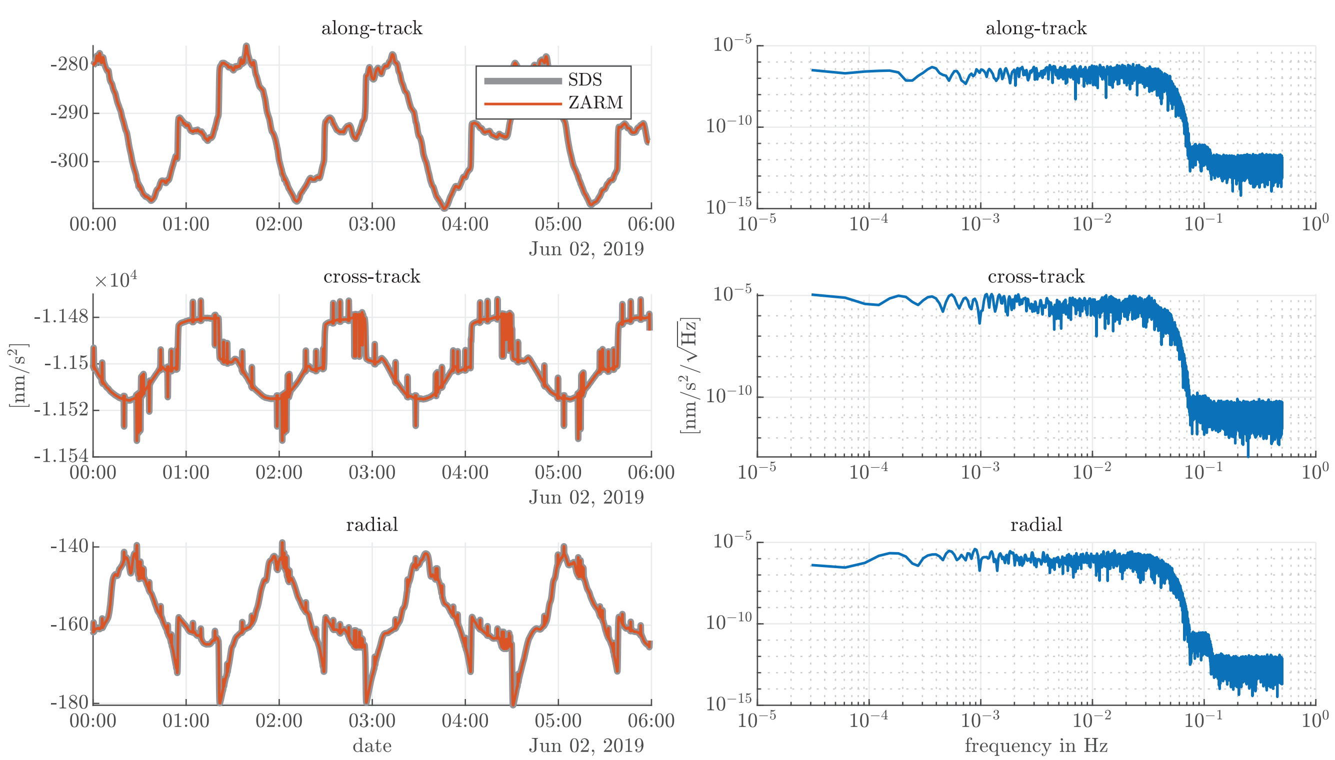

Fig. 4. Comparison between ZARM ACT1B and SDS ACT1B for GRACE-C on 2 June 2019. On the left the comparison of both data sets as time-series is given per SRF axis (along-track, cross-track and radial). On the right, the differences between the data sets is given in per axis in the frequency domain.

Table 1
Summary of considered non-gravitational perturbation models and their main parameters.

Perturbation	Models	Parameters
SRP	GFO-FEM, SOLAARS-CF	Solar Flux at 1AU, $q_{\odot} = 1367\,\mathrm{W/m^2}$
ALB	GFO-FEM	CERES SYN1deg-1H TOA Albedo, $q_{\odot}$
IR	GFO-FEM	CERES SYN1deg-1H TOA Longwave flux
TRP	GFO-FEM, *pde* temperature	c_p, ρ, h, λ cf. Table 3
Drag	GFO-FEM, var. C_D, HWM14, JB08/NRLMSISE-00	$C_D, f_{10.7}, a_p, \rho_{atm}$

Table 2
Summary of optical surface properties of the GFO components.

Comp	Emiss	Absorp	Refl (IR)		Refl (Vis)	
	ε	α	ρ_s	ρ_d	ρ_s	ρ_d
F/B	0.62	0.34	0.23	0.15	0.400	0.260
SA	0.81	0.65	0.03	0.16	0.050	0.300
Bottom	0.75	0.12	0.19	0.06	0.680	0.200
Boom	0.62	0.34	0.23	0.15	0.400	0.260
SCA	0.89	0.97	0.04	0.07	0.015	0.015
Antenna	0.90	0.18	0.01	0.09	0.020	0.800

F/B: Front/Back, SA: Solar Array, SCA: Star Camera Assembly

Table 3
Summary of material properties of the GFO components.

Component	c_p [J/kgK]	ρ [km/m^3]	λ [W/mK]	h [mm]
Front/Back				
Kapton	1095	1400	0.200	0.1
Insulation	1000	33	0.023	40.0
Honeycomb	900	45	0.080	30.0
Solar Arrays				
Solar Panel	540	2000	1.850	2.5
Insulation	1000	33	0.023	40.0
Honeycomb	900	45	0.080	30.0
Bottom				
Teflon	1095	1400	0.200	2.0
Insulation	1000	33	0.023	40.0
Honeycomb	900	45	0.080	30.0
Boom				
Kapton	1095	1400	0.200	0.1
Aluminium	900	2700	237.000	2.5
Star Camera				
Aluminium	900	2700	237.000	5.0
Insulation	1000	33	0.023	40.0
Antenna				
CFRP	1040	2000	60.000	2.0
Insulation	1000	33	0.023	40.0
Honeycomb	900	45	0.080	30.0

their main parameters can be found in Table 1. The list includes solar-radiation pressure (SRP), Earth Albedo radiation pressure (ALB), Earth infrared radiation pressure (IR), thermal-radiation pressure (TRP) and atmospheric drag. All presented results in this chapter are for the GRACE-C satellite as the satellite's accelerometer is an excellent reference for our simulated data and allows assessment of the performance for the other satellite.

3.1. Finite element model

In the XHPS, the accelerations acting on a satellite are calculated with the utilization of a finite element (FE) model of the satellite. The FE models used here are based on dimensions and parameters given in (Wen et al., 2019). Two models were created for different purposes. One model is more detailed to get most precise results, where as the other is less detailed with less number of elements to realize a compromise between precision and computational effort. In addition to the listed components in Wen et al. (2019), the finite element models were extended by the star camera assembly as well as K-band ranging (KBR) and Global Positioning System (GPS) antennas. For these components assumptions about material and optical surface properties have been made. Based on available photos during assembly, it was assumed that the funnel in which the star cameras are recessed is made from aluminium. The antennas were assumed to be some kind of fibre reinforced composite material. The colour of the components defines the optical surface properties, therefore the aluminium was assumed to be coated with black paint and the antennas with white paint. A full list of the optical properties is given in Table 2. The surface temperature is dependent on the material properties density (ρ), specific heat capacity (c_p) and thermal conductivity (λ), which are listed in Table 3.

The two FE models are shown in Fig. 5 including a depiction of the illumination condition for an arbitrary radiation incident direction. For the geometry of GFO, a shadowing on the bottom of the satellite can occur. This has a non-negligible impact on the radiative forces acting on the satellite.

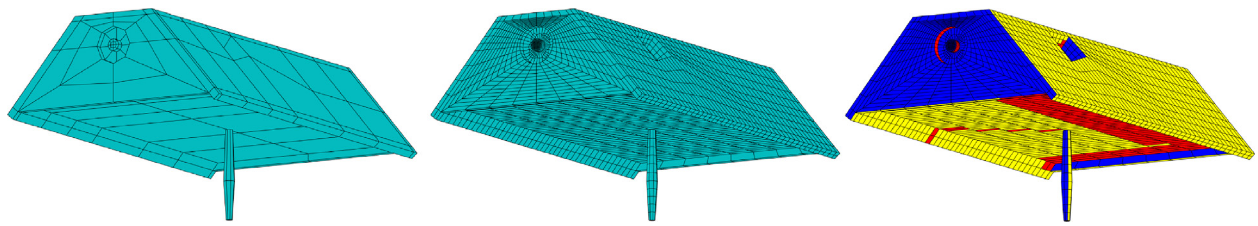

Fig. 5. (Left, middle) Simple and detailed FE model. (Right) Illumination conditions of the detailed FE model for one incident direction, yellow: illuminated, blue: not illuminated, red: shadowed.

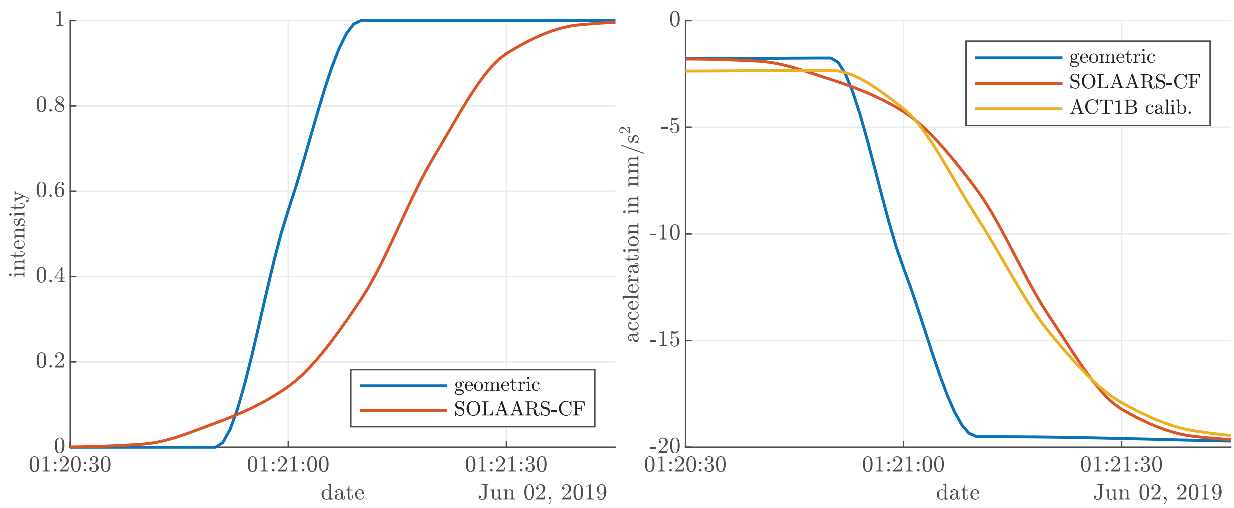

(a) Intensity factor of solar radiation.

(b) Comparison of modelled acceleration and calibrated ACT1B.

Fig. 6. Comparison of geometric and SOOLARS-CF eclipse models for an exemplary eclipse transition period on 2 June 2019.

3.2. Solar radiation pressure

The calculation of the solar radiation pressure is the perturbation with the least computational effort. We consider the Sun as a point source that emits an average heat flux q_{in} of 1376 W/m^2 at one AU. The acceleration due to solar radiation can be calculated as the sum over all FE elements k:

$$\mathbf{a}_{SRP} = -\frac{q_{in} f_e}{m_{sat} c} \sum_k f_{sh,k} A_k \mathbf{e}_{inc} \cdot \mathbf{e}_{N,k} \cdot \left[(\alpha_k + \gamma_{d,k}) \mathbf{e}_{inc} + 2\left(\frac{\gamma_{d,k}}{3} + \gamma_{s,k} \mathbf{e}_{inc} \cdot \mathbf{e}_{N,k}\right) \mathbf{e}_{N,k} \right]. \quad (3)$$

The unit vectors $\mathbf{e}_{inc}$ and $\mathbf{e}_{N,k}$, describe the incident direction of the solar flux and the element normal vector, respectively, c describes light speed, m_{sat} the satellite's mass and A_k the element area. The optical surface properties $\alpha_k, \gamma_{d,k}$ and $\gamma_{s,k}$ define the amount of absorbed, defuse and specular reflected radiation, respectively. The remaining variables are the binary factor $f_{sh,k}$, which defines if a FE element is illuminated or not, and the factor f_e describing the eclipse condition as a number between 0 (night side) and 1 (day side). The XHPS includes two eclipse models: one geometric based on the radii of the source and the obstructing body as well as their distance and the satellite orbit and one also regarding light refraction in Earth's atmosphere. The second model is the Solar radiation pressure with Oblateness and Lower Atmospheric Absorption, Refraction, and Scattering Curve Fit (SOLAARS-CF) method developed by Robertson (2015). The comparison of the SOLAARS-CF and the geometrical eclipse model in the modelled accelerations to daily-bias calibrated ACT1B data are illustrated in Fig. 6. It can be seen that the transition from full eclipse to full exposure takes about twice as long for the SOLAARS-CF model compared to the geometric one. This leads to a better agreement of the modelled acceleration with the calibrated accelerometer data than with the geometric model.

3.3. Thermal radiation pressure

Thermal radiation pressure is a perturbation originating at the satellite. This acceleration is induced by absorbed and internally generated heat yielding a non-uniform temperature distribution over the satellite's surfaces. The thermal radiation is governed by the partial differential equation for the temperature of each FE element k:

$$c_{p,k} \rho_k \frac{\partial T_k}{\partial t} = \lambda_k \frac{\partial^2 T_k}{\partial x_k^2}. \quad (4)$$

with heat capacity $c_{p,k}$, material density ρ_k, material thickness h_k, surface temperature T, time t, absorbed radiation flux $q_{abs,k}$, emissivity ϵ_k, and the Stefan–Boltzmann constant σ. For a detailed description of the different temperature models and calculation procedures the reader is again referred to Wöske et al. (2019). The material parameters of the satellite components are listed in Table 3 for completeness. For each component the wall is modelled as multiple layers with different properties and thicknesses.

3.4. Aerodynamic accelerations

The acceleration due to residual atmosphere at the satellite's positions acts mostly in opposite direction of the satellite's velocity vector, therefore the aerodynamic acceleration is widely called atmospheric drag. Lift as well as side accelerations are often neglected. Depending on the atmospheric models utilized in the simulation tool, we are able to calculate a dedicated lift acceleration.

The atmospheric drag can be calculated according to the following equation, where A_{proj} denotes the cross-section area of the satellite normal to the incident direction, C_D the drag coefficient, ρ the atmospheric density, m_{sat} the satellite's mass, v_{inc} and $\hat{\mathbf{v}}_{inc}$ the incident velocity of the atmosphere on the satellite and it's unit direction vector, respective

$$\mathbf{a}_D = -\frac{\rho C_D A_{proj} v_{inc}^2 \hat{\mathbf{v}}_{inc}}{2m_{sat}}. \tag{5}$$

The incident velocity $\mathbf{v}_{inc}$ combines the inertial velocity of the satellite $\mathbf{v}_{sat,i}$ with the horizontal wind velocity $\mathbf{v}_{HWM,i}$ obtained from the HWM14 (Drob et al., 2015). The horizontal wind velocity is given in local coordinates and the transformation from local to inertial reference frame includes the term $\omega_E \times \mathbf{r}_{sat,i}$, which describes the velocity of the co-rotating atmosphere. To model the non-gravitational accelerations acting on the satellites as accurately as possible, we investigated the performance of multiple atmospheric models as well as incorporations of the drag (and lift) coefficient. Their results are briefly presented in Section 3.5. The considered atmospheric models are the Jacchia-Bowman 2008 (Bowman et al., 2008) and NRLMSISE-00 (Picone et al., 2002). A third empirical and commonly used model is the DTM model (Bruinsma, 2015) which is not investigated, because it is not part of the simulation tool, yet. Incorporation of this model is planned for the future, due to discovery of its favourable performance at other processing centres.

One incorporation of the drag coefficient is done as a constant factor of 2.4, according to its shape and in agreement with the publication of Behzadpour et al. (2021). The other incorporation is a variable drag coefficient calculation based on free molecular flow interactions at the satellite's surfaces (Sentman, 1961; Doornbos, 2011). The free molecular flow model is a aerodynamic approach considering the rarefied atmosphere and particle surface interactions in the thermosphere. It is not a classical aerodynamic model based on Navier–Stokes equations but is believed to be more physically correct. With this approach also a lift coefficient C_L and the acting direction of the lift acceleration $\hat{\mathbf{n}}_L$ can be determined, which are combined in the following lift equation:

$$\mathbf{a}_L = \frac{C_L A_{proj} \rho v_{inc}^2 \hat{\mathbf{n}}_L}{2m_{sat}}. \tag{6}$$

The $\hat{\mathbf{n}}_L$ vector is located in a plane perpendicular to the $\hat{\mathbf{v}}_{inc}$ vector and its precise orientation in this plane is determined by the sum of the normal vector of every contributing finite element of the satellite model (Doornbos, 2011). Due to the incident velocity of the atmosphere with respect to the satellite in Eq. 5, the drag acceleration not only acts in SRF x-axis, but also in y- and z-axis. Similar for the lift, which mainly acts in negative/positive z-axis for the trailing/leading satellite, but also has contributions in x- and y-axis. It has to be noted that the lift is significantly smaller than the drag acceleration. The variable coefficients can only be calculated in combination with the NRLMSISE-00 due to the necessary information of the atmospheric composition.

3.5. Data validation

Validation of the simulated acceleration data is done by comparison to daily-bias calibrated thruster-free accelerometer data ($ACT1B_{woTHR}$). We limit the calibration to a daily-bias estimation, to ensure that model errors are not fitted into calibration parameters. However with a scale estimation, the measured data is easily adjusted to the simulated data. For the sake of readability the calibrated accelerometer data is denoted with ACT_{cal}, calculated from the following equations:

$$ACT_{cal} = \mathbf{s}ACT1B_{woTHR} + \mathbf{d}t + \mathbf{b}, \tag{7}$$

where $\mathbf{b}$ denotes the bias vector, t the time in seconds since beginning of calculation and $\mathbf{d}$ and $\mathbf{s}$ the drift and scale vector, respectively. Here, the drift and scale vectors are set to zero and unity, respectively. A standard least square equation can be set up as follows:

$$\min \|ACT1B_{woTHR} + \mathbf{b} - ACC_{sim}\|^2, \tag{8}$$

which can then be rearranged to estimate the bias vector:

$$\mathbf{b} = \left(X^T X\right)^{-1} X^T (ACC_{sim} - ACT1B_{woTHR}), \tag{9}$$

where X is a vector of ones. Residuals for each data point can then be calculated as:

$$\mathbf{r} = ACC_{sim} - ACT_{cal}. \tag{10}$$

The first comparison is done in terms of daily root mean square (rms) values of the residual vector $\mathbf{r}$ for all three axes as time series. Fig. 7 shows the residuals $\mathbf{r}$ for GRACE-C for one year. The three data sets are generated with different combinations of density values from the JB08 and NRLMSISE-00 atmospheric models and a constant or

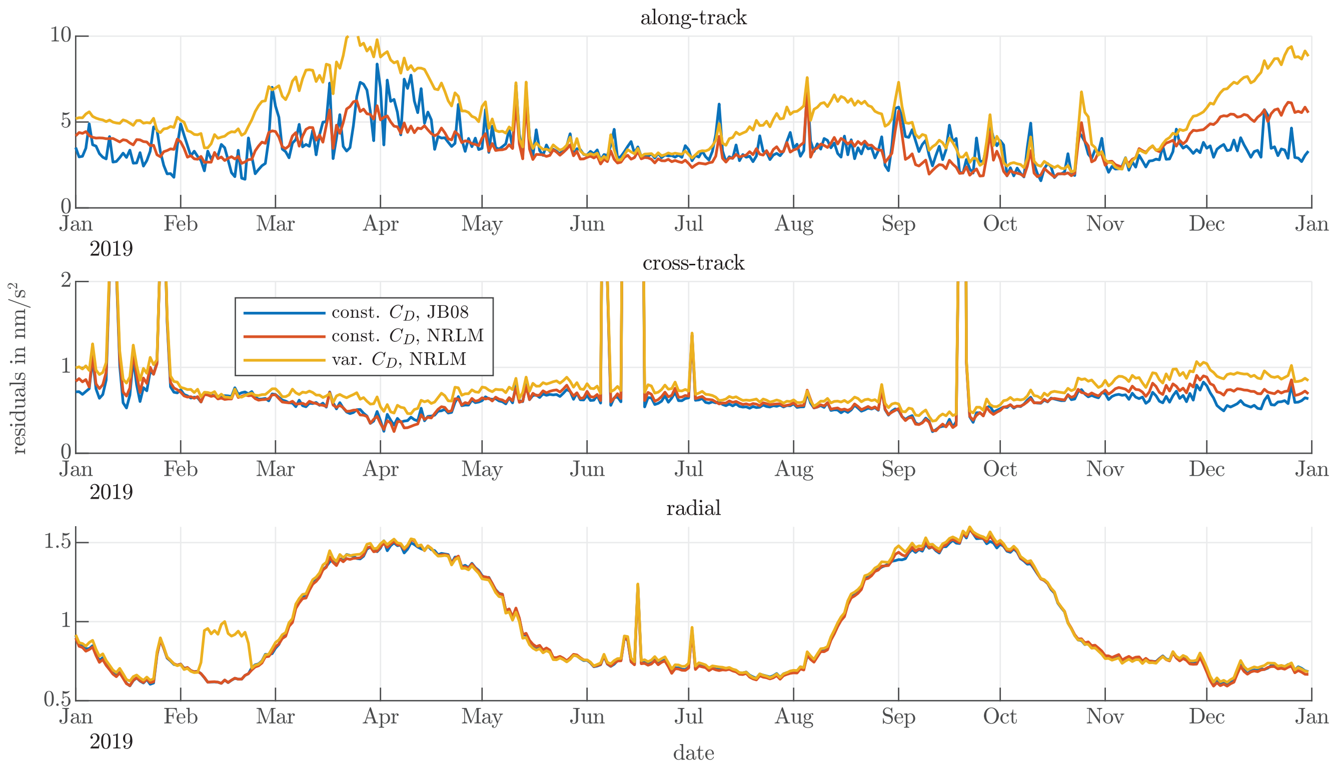

Fig. 7. Daily root mean square values for 2019 of the difference in SRF axes between the bias calibrated SDS ACT1B data and our modelled acceleration data with different model combinations for GRACE-C.

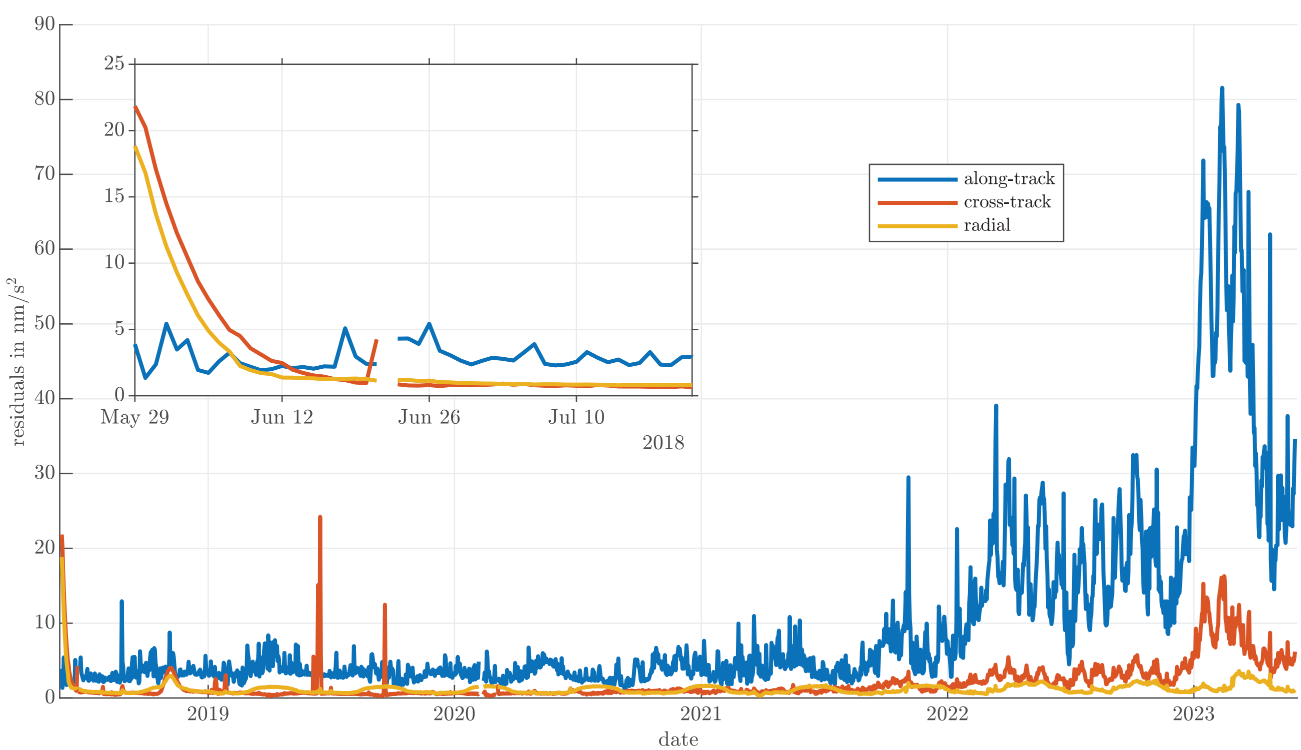

Fig. 8. Daily rms values of the difference between bias calibrated SDS ACT1B and modelled acceleration data from May 2018 to May 2023 and GRACE-C. Gap in data on 22 June 2018 due to collision avoidance manoeuvrer (JPL, 2023).

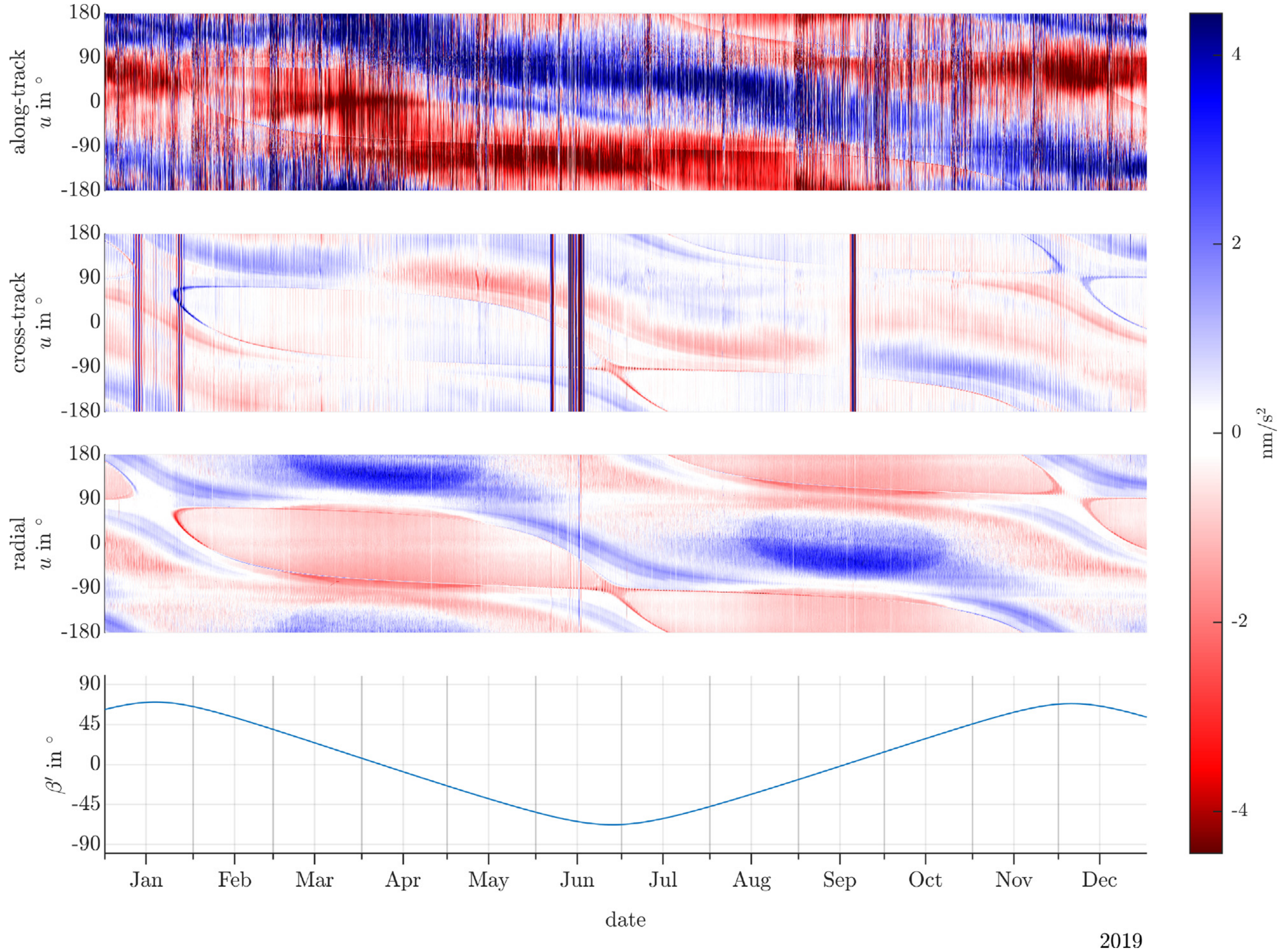

Fig. 9. Residuals for 2019 of simulated data with JB08 and const. C_D to calibrated accelerometer data for GRACE-C in the three SRF axes. Additionally, the β' angle shows the dependency of the residuals to the orientation of the orbital plane to Sun.

variable drag coefficient, according to Eq. 5. The data generated with variable drag coefficient and NRLMSIS-00 also includes the lift acceleration based on the variable C_L, which evidentially has no significant impact on the residuals in z-axis apart from a short period in February, where the satellite was in nadir-pointing mode. However, this artefact is caused by a particularity of the calculation algorithm and needs to be further investigated regarding its plausibility.

Generally, it can be seen that the residuals of the bias calibration are lower for the y- and z- than for the x-axis. On certain dates, some satellite operations like temperature calibration (e.g. 12–15 June 2019, (Webb et al., 2019)) lead to high drifts in the accelerometer data. These occurrences are visible in the data as outliers due to our daily-bias calibration and not due to errors in our simulation.

Regarding the residuals in the x-axis, the influences of the different atmospheric models as well as the variable drag coefficient can be seen. The daily variation of the rms values is lower with the NRLMSISE-00 model than with the JB08 model (red and blue graph). The variable drag coefficient leads to higher residuals (yellow graph), dependent on the beta prime β' angle, which describes the orientation of the orbital plane to the Sun. For periods around zero degree for β', the variation with orbit frequency in both density and variable C_D increases, which are not absorbed into the daily bias. The variable C_D method introduces continuously higher values than the shape-based values traditionally chosen. This is in agreement with the dissertation of Doornbos (2011), nevertheless the reason behind the higher residuals is currently jointly investigated with the lift artefacts in more detail. This includes the influence of the accommodation coefficient and surface area of the satellite.

Fig. 8 shows the daily rms residuals for the mission duration from May 2018 to May 2023 for the constant drag coefficient and JB08 combination. Only one model combination is chosen to be presented here, as the relative performance between all model combinations shown in Fig. 8 for 2019 preserves for most of the mission duration. During periods of nadir pointing in early 2023 we again see artefacts from the variable C_D and C_L model, which are under investigation.

The zoom-in pictures the elevated residuals in y- and z-axis due to an outgassing effect which is not modelled in our simulated data. The most prominent behaviour are the increasing residuals in x-axis from mid 2021 onwards. This is due to the increasing solar activity and the consequently worse performance of the atmospheric model. With increasing solar activity the shares of the drag acceleration in y- and z-direction also become more prominent, as their residuals rise as well. Additionally a signal with approximately two revolutions per year is visible, which can be ascribed to the dependency of our data to the orbital orientation or beta prime angle β'. This dependency is explained in more detail for Fig. 9.

A spatial and temporal illustration of the residuals is realized by argument of latitude plots. The argument of latitude u is the sum of the true anomaly v and the argument of periapsis ω (Prussing and Conway, 1993, 48 f.):

$$u = v + \omega. \tag{11}$$

The residuals for the combination of the JB08 model and a constant C_D are shown in Fig. 9. A dependency of the residuals to the beta prime β' angle in y- and z-axis can be identified. An angle of 90° describes the perpendicular orientation of the orbital plane to the direction from Earth to Sun.

In the z-axis the residuals are more prominent for times with a beta prime angle of around zero, whereas they are less prominent for those times in the y-axis. In the z-axis, also the instances of transitions into or out of the eclipse can be determined, which are the lines of the highest residuals at about −90° and 90° of u. The opposing dependency of the residuals to β' can be ascribed to two factors. For one, the residuals are absolute values and not relatives of the acceleration, which means that the residual magnitude varies with the acceleration magnitude. And second, the residuals per axis also depend on β'. For a beta prime angle of 0° the satellite is illuminated exclusively in the xz-plane of the SRF, whereas the illumination direction changes more towards the positive or negative y-axis of the SRF with β' diverging from 0°. This leads to nearly vanishing residuals in y-axis for $\beta' = 0°$.

The comparison of simulated and real acceleration data showed the overall quality of our modelling but also its limitations. The limiting factor is the atmospheric drag modelling, which results in residuals of up to 20 nm/s^2 in the SRF x-axis for single dates, whereas the residuals never exceed 2 nm/s^2 in the other two axes. This means the accelerometer precision is not reached for any of the axes, but the comparison for GRACE-C validates our environment modelling in general. The radiation models contributing mostly in y- and z-axis are highly accurate and show an unvarying, good performance. The drag modelling is the limiting factor of our simulation, which becomes especially apparent for days of higher solar activity in 2022 and later. For these dates the share of the drag acceleration increases in all axes and residuals rise accordingly. Error analyses of our incorporated models are not included here because they are part of a future publication, already in preparation. The interested reader is referred to Wöske et al. (2019) for analyses regarding the precision of some of the models applied for accelerometer simulation of the GRACE satellites.

The environment modelling procedure is not limited to GRACE Follow-On but can be applied to any space mission with publicly available orbit and satellite geometry data.

4. Investigation of artificial data for GFR

In this chapter we present estimated gravity fields based on our modelled data for GRACE-D for January 2019. We generate these fields with our in–house processing tool, which uses the classical time-wise variational equation approach (Wöske, 2021), as well as with the Gravity Recovery Object Oriented Programming System (GROOPS) (Mayer-Gürr et al., 2021). GROOPS is a C++ software toolkit for performing core geodetic tasks developed at the Graz Technical University (TUG) and the tool the ITSG-operational gravity fields are generated with.

We utilize our in–house tool to be able to investigate the whole process chain from data generation to final gravity field. In this tool we can investigate the influence of different parametrizations and the importance of certain parameters for our data. Additionally, GROOPS is used to generate solutions for two reasons. First, it enables us to benchmark our in–house tool to a state-of-the-art gravity field recovery tool and second, the results with the renowned GROOPS software tool are of greater value to the Geodesy community.

A performance comparison of our modelled to actual accelerometer data in gravity field determination can not be done, due to the early corruption of the data from the GRACE-D accelerometer and outgassing of the satellites in the earliest mission days. The outgassing leads to a drift in the residuals to daily-bias calibrated accelerometer data (see the enlarged box in Fig. 8). This leaves only a small number of accessible dates with real accelerometer data for both satellites insufficient for a comparable gravity field determination. Nevertheless, a comparison of our modelled data to the transplants of JPL and TUG is made for 2019.

For utilization in gravity-field recovery the modelled data has to be combined with the thruster-only data obtained during the L1A to L1B processing. The 1 Hz thruster data does not display the actual accelerometer response to thruster firings due to the applied CRN filter. A simulation study performed in Section 8.8 of Wöske (2021) showed that it has no influence on gravity field solutions if unfiltered or filtered thruster data is used. Due to the availability of both L1A and L1B thruster data from the accelerometer data processing, we generated gravity field solutions with both unfiltered and filtered thruster data. For this we utilized GROOPS and could show that the thruster data has an influence for GRACE-FO as pictured in Fig. 10. The degree variance quality decreases for unfiltered thruster data, therefore all following gravity field solutions utilize CRN-filtered thruster data.

A monthly ITSG solution is presented as an overall reference for our gravity field solutions here and in the following sections, as it is considered the state-of-the-art gravity field solution. The monthly ITSG solution (Kvas et al., 2019) and the TUG transplant ACT1B (Behzadpour et al., 2021) are obtained from the ftp server (ftp.tugraz.at/outgoing/ITSG/GRACE/) of the TUG. The JPL ACT1B and ACH1B data is obtained form the Information System and Data Center (ISDC) ftp server (ftp://isdcftp.gfz-potsdam.de/grace-fo/Level-1B/JPL/INSTRUMENT/RL04/) (JPL, 2019).

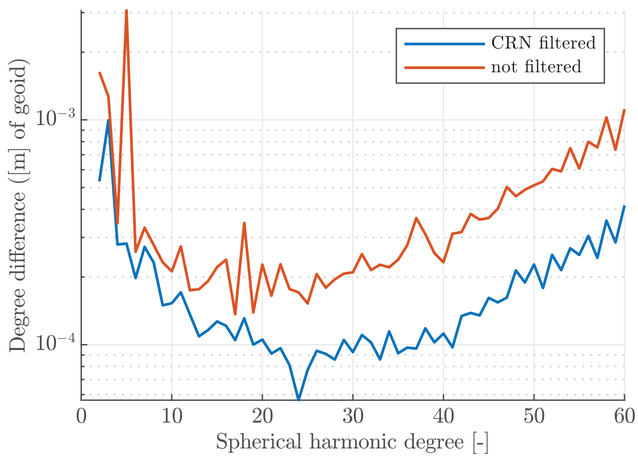

Fig. 10. Degree difference plot of gravity field solutions from GROOPS for January 2019 with unfiltered and filtered thruster data.

Fig. 11 shows degree-difference plots of the gravity field solutions for the different data sets and estimation parameters for January 2019 with respect to a mean 2019 GOCO06s gravity field (Kvas et al., 2021) from the in–house (Fig. 11) and GROOPS tool (Fig. 11b). In the in–house tool, co-estimated accelerometer calibration parameters in the recovery process are either bias and scale or bias and drift, referred to as *bs* and *bd*, respectively, and are estimated constant per three hour arcs. Simultaneous co-estimation of all three parameters is not investigated here, as it was identified to be not advantageous in the in–house processing tool in Wöske (2021).

Eight of the nine presented solutions in Fig. 11a utilize the JPL ACT1B data for GRACE-C, the ninth solution is generated with simulated data for both satellites. The solutions with the *bd* estimation parameters are visible at the very top of the graph, indicating significantly higher

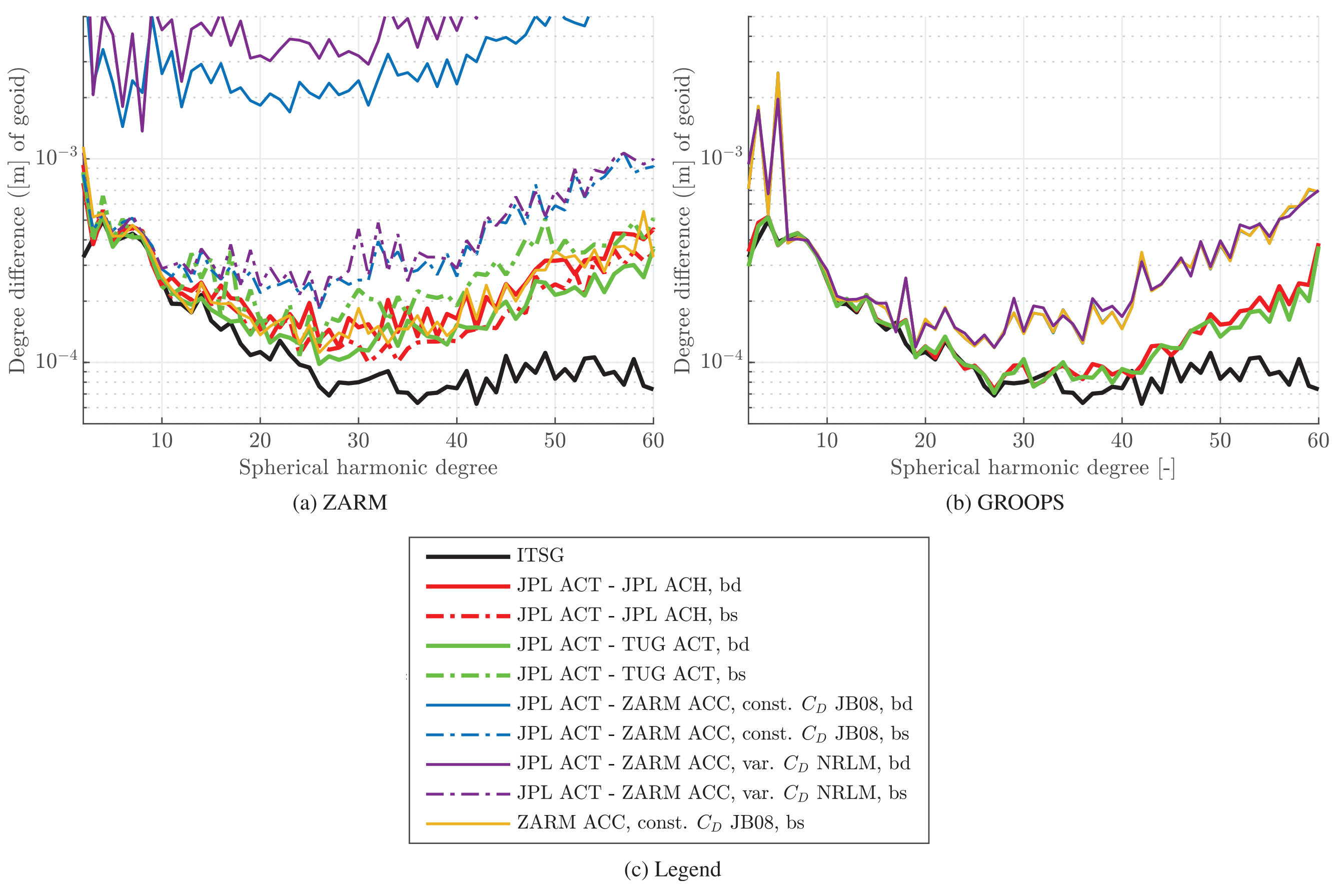

Fig. 11. Degree difference plots of gravity field solutions for January 2019 with ZARM processing tool and GROOPS. ITSG of January 2019 as reference. bd: bias/drift, bs: bias/scale.

degree differences than all other solutions. For all solutions with a combination of real and simulated data *bs* (dashed lines) performs better than *bd* (solid lines), therefore scale is the more important estimation parameter in combination with our simulated data. This is mostly due to the modelling errors in the atmospheric drag calculations, which leads to mismatched data sets for GRACE-C and -D. In the GFR process the accelerations and KBR measurement have to be fitted to one another and a scale factor can compensate for the modelling error.

For the solutions with transplant data from JPL and TUG, the difference between *bd* and *bs* is significantly smaller, with *bs* performing slightly better for JPL and *bd* performing better for TUG. The reduced significance of the co-estimated parameters can be explained by the transplant procedure. In the TUG transplant, for example, a corrective factor related to atmospheric density and drag coefficient is estimated and transplanted (Behzadpour et al., 2021). This procedure can be compared to a calibration including scale prior to the GFR process, which reduces the difference of modelled GRACE-D and real GRACE-C acceleration. Therefore, the importance of *bs* or *bd* is significantly smaller for the TUG transplant data than for our modelled data.

The result of a combination of two simulated data sets shows the potential of the artificial accelerations. Here, no mismatch between acceleration data of GRACE-C and -D is present and the GFR process is able to better combine all observations. With this, an improved gravity field estimation compared to combination of real and artificial acceleration data can be achieved that is comparable to the ACH1B or TUG transplant results.

Regarding the differences between the combinations of constant C_D with JB08 and variable C_D with NRLMSISE-00, it can bee seen that the solutions are very similar. A slightly favourable performance of const. C_D with JB08 over var. C_D with NRLMSISE-00 can be identified. However, the best performing combination varies from month to month, so that no statement about a suitable combination for gravity field determination can be made at this point. Therefore, both combinations are further investigated in the transplant generation and subsequent gravity field determinations.

In Fig. 11b we present gravity field estimations with the same data combinations as before generated with GROOPS. The example for GRACE gravity field recovery provided for users at the GROOPS github webpage is used. The provided GRACE example setup differs from the ITSG operational setup for example in the following, which are responsible for the higher degree differences of the solution with the TUG transplant compared to the ITSG (Öhlinger, 2023):

- no utilization Land Surface Discharge Model (Dill, 2008),
- temporal parametrization of lower degree and longer period,
- no consideration of SST special events like eclipse transitions and Sun intrusions (Behzadpour et al., 2019),
- different autoregressive (AR) model, short time variation constraint (Kvas and Mayer-Gürr, 2019).

Both Figs. 11a and 11b show the same *y*-axis for the degree differences, therefore results from the in–house tool and GROOPS can be directly compared. The GROOPS tool is used as setup by TUG, therefore no investigation about performance of different accelerometer calibration parameters are made. The colour code represents the same model combinations as in Fig. 11a. The extend of the utilized calibration parameters are listed in Table 4.

It can be seen that solutions from GROOPS show overall lower degree differences, as expected. Solutions with combinations of real and our modelled data are equally similar as with our in–house processing. Surprisingly, they show higher degree difference for the degrees three and five than any other solution apart from the two *bd* solutions from our in–house tool. Up to degree 15 the solutions are very similar to the transplants before they slowly diverge for higher degrees.

What is most interesting about the GROOPS solutions are the virtually identical results for the two const. C_D JB08 solutions (blue is covered by yellow graph). Therefore, in GROOPS no improvement is achieved by utilizing artificial data for both satellites, which shows the superiority of GROOPS over our in–house GFR tool. At this point only educated guesses regarding the processes responsible for the better performance can be made. Differences between the gravity field recovery tools have been listed in Table 4. Overall, one can say that GROOPS uses a highly stronger parametrization which is capable of compensating the differences between real and artificial acceleration data.

The results show that combinations of real and artificial data can be used in gravity field recovery, but they also show the limitation of achievable quality. To increase the quality, we develop a minimalistic transplant procedure which corrects the acceleration data in the *x*-axis by applying estimated density values from GRACE-C to GRACE-D with a time-shift. Hence we use a physically motivated estimation parameter and not a stochastic parameter to reduce the residuals.

Table 4
Differences of gravity field recovery tools.

GROOPS	ZARM
Fully populated scale matrix	Diagonal scale matrix
Acc. bias splines with 6 h nodes	3 h constant values
Kinematic and dynamic orbits	Dynamic orbits
AR model to constrain short-time variations of gravity field	No constrains of short-time variations
Weighting of single data points	Weighting of data sets
Full covariance matrix of observation data and models	No covariance matrix

The solutions utilizing artificial data for both satellites are promising for the generation of gravity field solutions for satellite missions without on-board accelerometer, at least for time periods with low solar activity. The increasing residuals visible in Fig. 8 support the hypothesis that the atmospheric model is the limiting factor of the artificial acceleration data. The potential of solutions with only artificial accelerometer data is reviewed for periods with higher solar activity and thermospheric density. Gravity field solutions for May 2023 with artificial accelerometer data show higher degree differences (see Fig. 26b in Section 7), which supports the limitation of artificial acceleration data in GFR for satellites without on-board accelerometers to periods with low solar activity.

5. Density estimation and transplant

The local thermospheric density is estimated from the accelerometer data of GRACE-C and then transplanted to GRACE-D by applying a time shift. This is done under the assumption that the satellites are following the same trajectory and temporal changes in density happening within the satellite's separation of maximum 30 s can be omitted. The density estimation procedure is inherited from another project in our working group, dealing with thermospheric density estimation from satellite accelerometer data (Wöske and Rievers, 2022; Wöske and Rievers, 2023).

First, we calibrate the GRACE-C thruster-free ZARM ACT1B with external calibration parameters obtained from a tailored precise orbit determination (POD). We use three hourly bias and constant scale factors. Second, the density is estimated through the residuals between the calibrated accelerometer and the simulated radiative acceleration data ($\mathbf{a}_{SRP}, \mathbf{a}_{ALB}, \mathbf{a}_{IR}, \mathbf{a}_{TRP}$). Using external calibration parameters has the advantage that no drag modelling errors from GRACE-C are transplanted to GRACE-D as opposed to using the simulated data with the a priori density from a model. This would result in a calibration that is based on the density that we want to determine. And hence applies a bias to the density that we want to estimate and transplant.

However, the POD calibration parameters in z-axis are less precise then in x- and y-axis. Therefore, different calibration options are investigated in the transplant procedure. The impact of the different calibrations are briefly discussed in Section 6.

For all calibration options we first consider Eq. 7 with external POD parameter:

$$ACT_{cal} = \mathbf{s}_{pod} ACT1B_{wothr} + \mathbf{b}_{pod}. \tag{12}$$

The first calibration variant stops at this point and is labelled *cal*. For the second variant, the resulting calibrated ACT (ACT_{cal}) from the POD calibration is calibrated again and therefore labelled *calcal*. Here, equations Eq. 7 - Eq. 10 are incorporated so that ACT_{cal} is calibrated with a daily bias vector to the simulated acceleration data:

$$\min \|ACT_{cal} + \mathbf{b} - ACC_{sim}\|^2. \tag{13}$$

Compare Eq. 13 to Eq. 8.

For the third variant, the GRACE-C JPL ACT1B is calibrated according to Eq. 7 - Eq. 10. The result is called $ACT_{cal,sim}$. Afterwards the x-axis values from the POD calibration ACT_{cal} are combined with the y- and z-axis from $ACT_{cal,sim}$ to generate a new calibrated data set. This variant has been labelled *mixcal*.

$$ACT_{mixcal} = \begin{bmatrix} ACT_{cal,x} \\ 0 \\ 0 \end{bmatrix} + \begin{bmatrix} 0 \\ ACT_{cal,sim,y} \\ ACT_{cal,sim,z} \end{bmatrix}. \tag{14}$$

The advantage of these double calibrations is that in x-axis we make sure no density modelling errors are fitted into calibration parameters due to the external POD parameters. Additionally, the y- and z-axis are improved by the second calibration. For the density estimation y- and z-axis have a very minor influence because drag is mainly acting in x-direction. Fig. 12 depicts the residuals of two calibrated ACT1B datasets to artificial acceleration data.The solid graphs represent residuals for the single calibration, whereas the dashed lines depict residuals for the mixed calibration. Solid and dashed lines of the same colour only differ in the bias from the second calibration. It can be seen that the residuals in z-axis for the *cal* variant are about an order of magnitude larger than for the *mixcal* variant. The y-axis shows only slightly different residuals whereas the x-axis residuals are identical. The reduced z-axis residuals impacts the estimated density due to the partial drag acceleration in this axis caused by the relative pointing of the satellite and the projection on the incident direction as described in the next paragraph.

The density is estimated from the calibrated accelerometer data ACT_{cal} according to the following approach, where ACT_{cal} can be replaced with any of the other calibrated ACT results. We assume the modelled radiation perturbations are highly precise and their errors are negligible

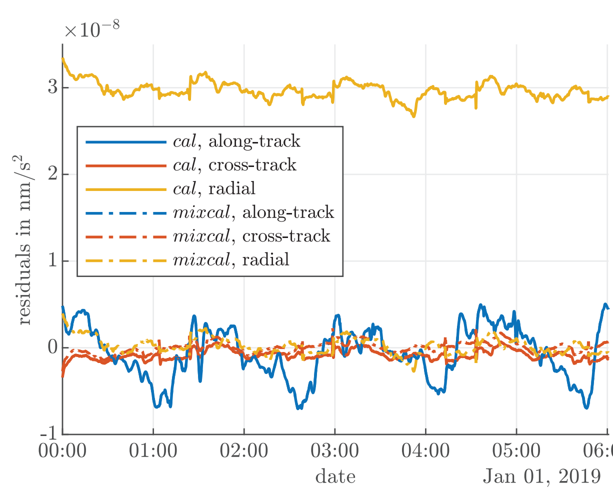

Fig. 12. Impact of second calibration on residuals for calibrated accelerometer to simulated acceleration data for GRACE-C.

compared to the error of the atmospheric modelling. Subtraction of the radiation accelerations from the calibrated accelerometer data yields a term that only contains aerodynamic accelerations:

$$\mathbf{a}_{aero} = ACT_{cal} - (\mathbf{a}_{SRP} + \mathbf{a}_{ALB} + \mathbf{a}_{IR} + \mathbf{a}_{TRP}). \quad (15)$$

To estimate the density this aerodynamic term is projected on the incident velocity direction. This velocity vector combines the inertial velocity of the satellite and the velocity of the atmosphere, as described in Section 3, which is the main acting direction of atmospheric drag:

$$a_{aero,proj} = \|(\hat{\mathbf{v}}_{inc} \cdot \mathbf{a}_{aero})\hat{\mathbf{v}}_{inc}\|. \quad (16)$$

The $\hat{\mathbf{v}}_{inc}$ denotes the unit vector of the incident velocity.

The projected aerodynamic acceleration can then be expressed as follows:

$$a_{aero,proj} = -\frac{A_{proj} C_D \rho \|\mathbf{v}_{inc}\|^2}{2m_{sat}}. \quad (17)$$

By rearranging this equation a density can be estimated under the assumption that all other parameters are known:

$$\rho_{est} = \frac{a_{aero,proj}}{k_D}, \quad (18)$$

where k_D is the reduced drag term:

$$k_D = -\frac{A_{proj} C_D \|\mathbf{v}_{inc}\|^2}{2m_{sat}}, \quad (19)$$

containing the cross-section area of the satellite normal to the incident direction A_{proj}, the drag coefficient C_D, the incident velocity vector $\mathbf{v}_{inc}$ and the satellite mass m_{sat}. The comparison between the modelled and estimated density from GRACE-C can be seen in Fig. 13. It becomes apparent, that the estimated density contains more high frequency variations, as well as slightly different course and magnitude compared to the NRLMSISE-00 model. The overall progression of the two estimated densities matches, whereas the actual value varies depending on using a constant or variable C_D in the density estimation. In Fig. 14 the influence of the calibration variations in the estimated density is shown for roughly two orbits. For this particular period, only differences between the *cal* and *mixcal* calibrations can be seen. The *calcal* graph coincides with the *mixcal* graph. The magnitude of the differences between the calibration options is smaller than the difference due to the constant or variable C_D model (compare to Fig. 13.), meaning the input C_D model has a larger influence on the estimated density than the calibration option. It has to be noted that the estimated density includes un-modelled errors from the radiative accelerations and all parameters in k_D, especially the modelled drag coefficient.

With the estimated density ρ_{est} a corrected drag and lift contribution of the non-gravitational perturbations can then be calculated. The sum of the radiation and the cor-

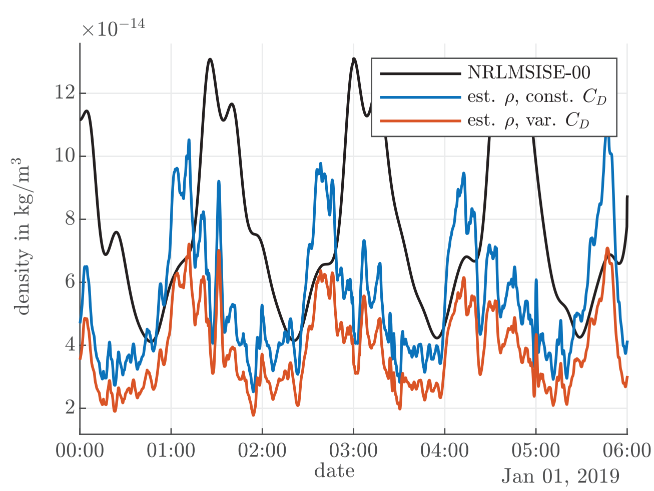

Fig. 13. Estimated density and modelled density from NRLMSISE-00 for GRACE-C.

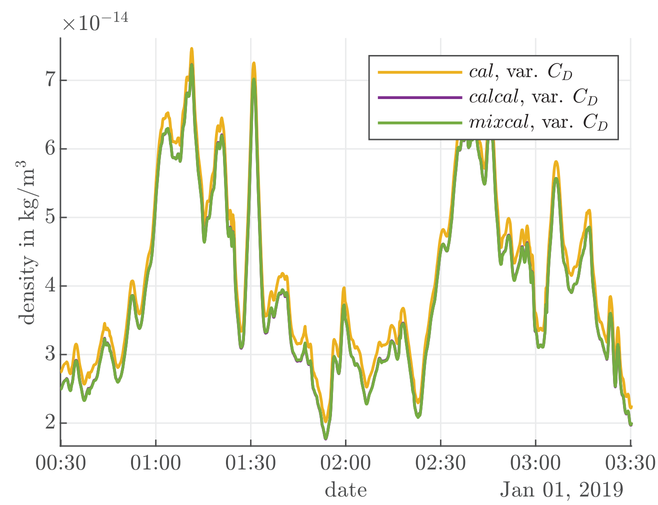

Fig. 14. Estimated density from NRLMSISE-00 for all calibration variations for GRACE-C. Note that *mixcal* graph covers *calcal* graph.

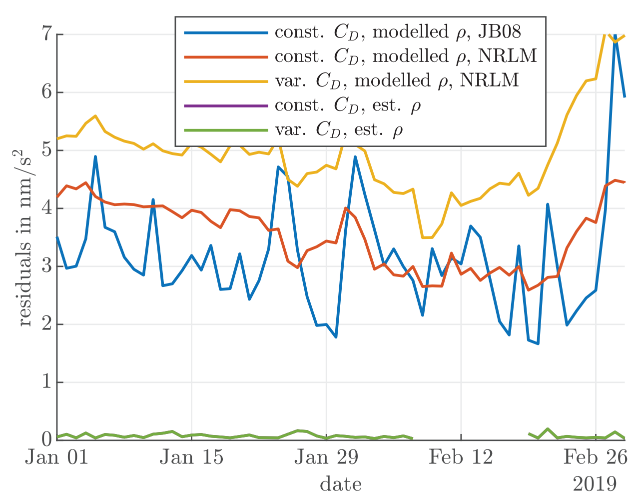

Fig. 15. Daily root mean square values of the differences in SRF x-axis of artificial acceleration data utilizing modelled and estimated density values with respect to daily-bias calibrated SDS ACT1B data for GRACE-C and January and February 2019. Data gap due to GRACE-D IPU shut off (JPL, 2023).

rected aerodynamic accelerations match the accelerometer data a lot better in the x-axis as can be seen in Fig. 15. The residuals for the two estimated densities are nearly identical, because density and C_D are multiplicative in the drag equation (Eq. 17) and hence compensate each other.

The correction procedure of the aerodynamic accelerations for GRACE-D starts with the determination of the time correction between the two satellites. We assume that both satellites pass the same location a certain time apart and the time delay can be calculated geometrically, if we accept some errors due to the following assumptions: Both satellites fly on the same orbit, which is circular. This introduces constant orbit radii and velocities for both satellites, whereas they actually are on slightly elliptic and different orbits with varying radii and velocities. These assumptions simplify the calculations considerably and introduce negligible errors in the interpolated density. Following this, we first calculate the circular arc connecting the two satellites, from their positions at the same time:

$$s = r_D \alpha, \quad (20)$$

where r_D is the vector norm of the position of the second satellite and α the angle between both positions:

$$\alpha = \arccos\left(\frac{\mathbf{r}_C \cdot \mathbf{r}_D}{r_C r_D}\right). \quad (21)$$

The time correction is given through the division of the circular arc by the velocity of the second satellite:

$$dt = \frac{s}{v_D}. \quad (22)$$

The time correction is then used to interpolate the density for GRACE-D from the estimated density of GRACE-C. Depending on which satellite is trailing or leading the sign of dt is either positive or negative. The time correction for one day of 2019 is shown in Fig. 16.

Fig. 17 shows the residuals for GRACE-D to the ACH1B transplant for the same period as for GRACE-C in Fig. 15. Compared to the GRACE-C residuals the decrease due to the estimated density is not as high for

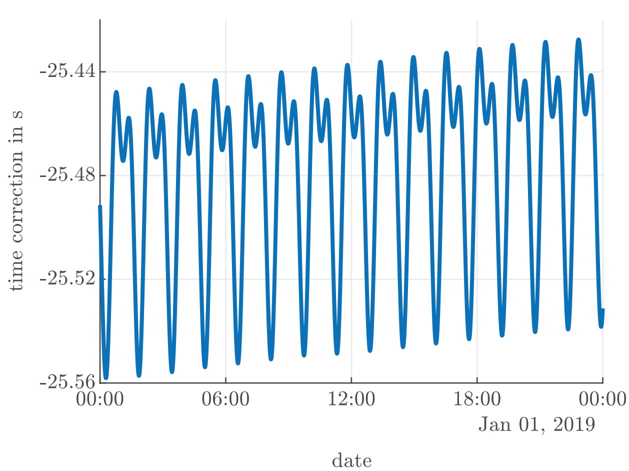

Fig. 16. Time correction between the two GRACE-FO satellites.

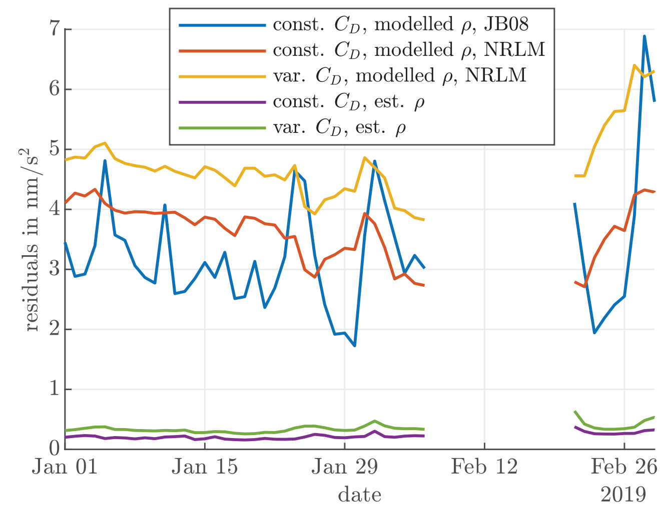

Fig. 17. Daily root mean square values of the differences in SRF x-axis of artificial acceleration data utilizing modelled and estimated density values with respect to daily-bias calibrated SDS ACH1B data for GRACE-D and January and February 2019. Data gap due to GRACE-D IPU shut off (JPL, 2023).

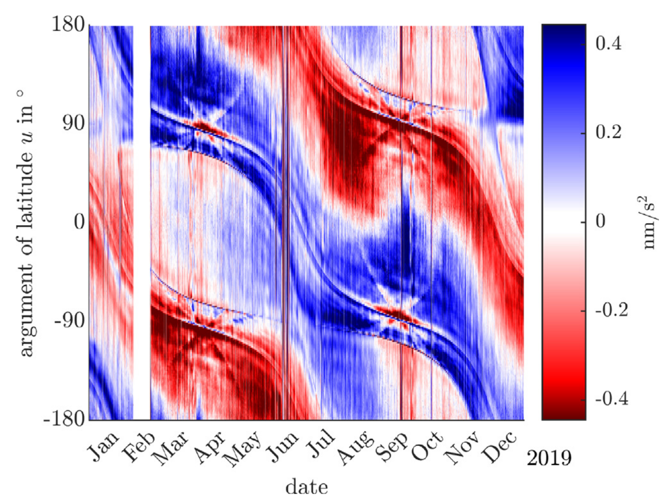

Fig. 18. Residuals for 2019 of transplanted data with JB08 and const. C_D to calibrated ACH1B data in the SRF x-axis.

GRACE-D but still significant and should improve our gravity-field solutions. Additionally, dedicated graphs for the estimated densities based on the input C_D model can be made out, which reflects the performance of the variable and constant C_D in the modelled data.

The spatial representation of the x-axis residuals for GRACE-D data in terms of an argument of latitude plot can be seen in Fig. 18 for the whole year of 2019. Compared to Fig. 9, where the residuals of the simulated data for GRACE-C are shown, one can see that the overall level in the x-axis was decreased by one order of magnitude. Additionally, the reduction of the level of residuals revealed more systematic errors. Whereas in Fig. 9 one can only vaguely see the dependency of the residual level to the beta prime angle over the argument of latitude, there are now multiple systematic errors visible. The cause of the star-like pattern has to be investigated, but might be related to multi reflections of radiation that occur for certain β' and incident radiation directions. For the distinct lines sweeping from top left to bottom right it was deduced that they represent the transition in or out of the eclipse and the fast changing illumination conditions.

The other two axes are barely influenced by the transplant process and therefore not depicted here. The influence of the chosen input models and variations in the transplant procedure on the transplant quality and gravity-field solutions are discussed in the next section.

6. Investigation of Transplant Procedure

6.1. GRACE Follow-On

The comparison of simulated data to ACT1B for GRACE-C in Fig. 7 showed large differences due to different drag modelling approaches. The differences from the atmospheric density models are equalized after the estimation of an atmospheric density, which is to be expected because every error made in the models is fitted into the density to best match the reference data. Only differences due to the C_D model and the calibration methods remain in the transplant acceleration data.

In Fig. 19 the residuals between the official JPL ACH1B transplant and the transplant data based on the three calibration variants and two C_D models are presented for GRACE-D. The variable C_D model also includes a lift term, which leads to the differences in z-axis, additionally to the expected differences in the x-axis. It can be seen that the C_D model has a greater influence than the calibration methods. The only distinguishable effect of *calcal* and *mixcal* options to the *cal* calibration is an over all lower level of the residuals in x-axis. In this figure, again outliers are visible at 12–15 June 2019 which are introduced through the transplant procedure from the drift in the ACT1B y-axis also into the x-axis. However, these outliers are significantly less prominent than in the y-axis. In the gravity field estimation process, arcs with lower quality data are automatically discarded or down-weighted, therefore no particular worse solution can be identified for June 2019 than for any other month.

The higher residuals for a variable drag coefficient in Fig. 19 entailed the attempt to estimate the drag coefficient as well. Therefore, the impact of a joint estimation of density and drag coefficient was investigated. If for the input model a constant drag coefficient is chosen, it makes no difference whether ρ or $C_D\rho$ is estimated, as the constant factor is absorbed in the multiplicative parameter and hence ρ is an indirect estimation of both parameters. Fig. 20 presents the residuals of our GRACE-D transplant data to official ACH1B data. Results for estimated ρ and $C_D\rho$ with both constant and variable C_D input are shown. The results are only given for one calibration variant as they are repre-

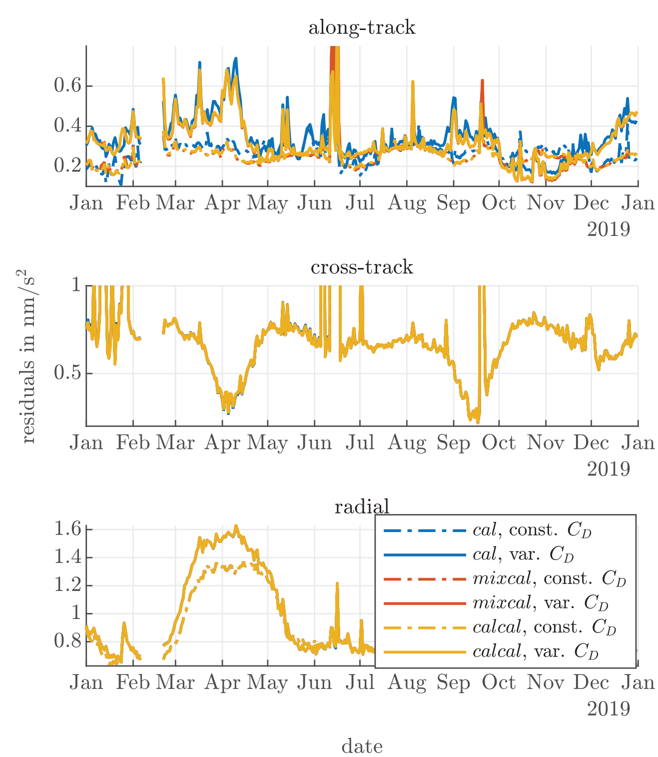

Fig. 19. Comparison of calibration procedures in terms of residuals from ZARM to ACH1B data for GRACE-D and the whole year of 2019.

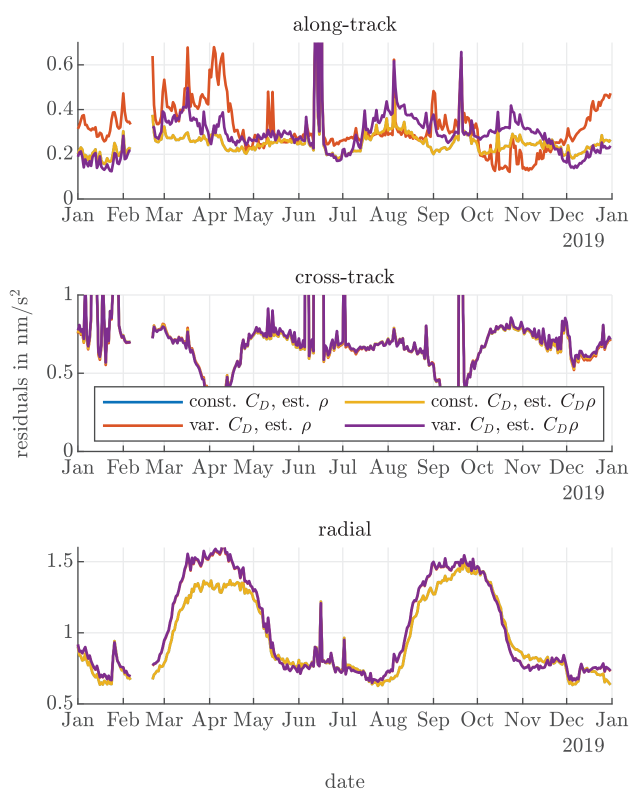

Fig. 20. Comparison of residuals of GRACE-D transplant data with estimated ρ and $C_D\rho$ to official ACH1B data. Results are for calibration variant *mixcal*.

sentative for the other two. It can be seen that the residuals in the SRF x-axis for variable C_D are generally higher than for constant C_D. The indifference of ρ or $C_D\rho$ estimation with constant C_D input is apparent by the yellow graph covering the blue one. On the other hand, the residuals for ρ or $C_D\rho$ estimation differ considerably for a variable C_D input model. In the first half of 2019, mostly estimation of $C_D\rho$ leads to lower residuals, where as in the second half the lower residuals are usually achieved by estimation of ρ.

In the SRF z-axis the residual are also higher for the var. C_D model but are more similar for the two estimation variations. This can be ascribed to the additional lift term which is also calculated with the estimated density. However, due to the combined estimation of ρC_D the density is not known as a separate value. The density can only be determined using the input C_D, which leads to errors from modelling assumptions.

6.2. GRACE

To verify the transplant procedure with real accelerometer data we apply it to the GRACE mission. Here, the accelerometer product is called ACC1B. The calibration method with a combination of external parameters from POD and calibration of the ACC1B to simulated data is the same as for GRACE Follow-On. A time correction between GRACE-A and -B is determined and the transplanted density applied to re-calculate the non-gravitational perturbations acting on GRACE-B. We investigate two time periods with different levels of solar activity. In 2003, the solar activity is near its maximum where as in 2009 it is near its minimum. Fig. 21 shows daily rms values of the x-axis residuals between daily-bias calibrated ACC1B data and the recalculated non-gravitational accelerations acting on GRACE-B for the month of March of both years.

It can be seen, that residuals using density from atmospheric models are overall higher for 2003, meaning the models perform not as good during high solar activity periods as during low solar activity. Which has also been shown for GRACE Follow-On in Fig. 8. The residuals using estimated and transplanted density values are also higher for 2003. Nevertheless, the transplant procedure reduces the residuals for both periods significantly. For 2009 the residuals are reduced to 20 to 40 % of the modelled values and during 2003 to 30 to 65 %. For 2003, the residuals using the transplant are varying more and the improvement is a little less prominent, but still show that the transplant procedure performs well for all periods.

Compared to the GRACE-D residuals in Fig. 17, the results for GRACE show less improvement due to the transplant procedure. This is expected, as the residuals for GRACE-D are with respect to ACT1B data that has been transplanted from GRACE-C, whereas the GRACE-B ACC1B data are actual measurements independent of GRACE-A. Therefore, modelling errors, for example in the drag coefficient, made at GRACE-A are more prominent at GRACE-B than the errors made for GRACE-C are at GRACE-D because of the dependency of D to C.

The investigation of the transplant performance for GRACE shows that the transplant procedure works and is predestined as a reference for improvements in the drag modelling in the future.

7. Transplant gravity field solutions

In this Section we present results from the gravity-field recovery for the whole year of 2019 as the basis for the discussion which transplant procedure and input model combination yields the best results. For February 2019 no gravity-field solutions have been calculated as there is data

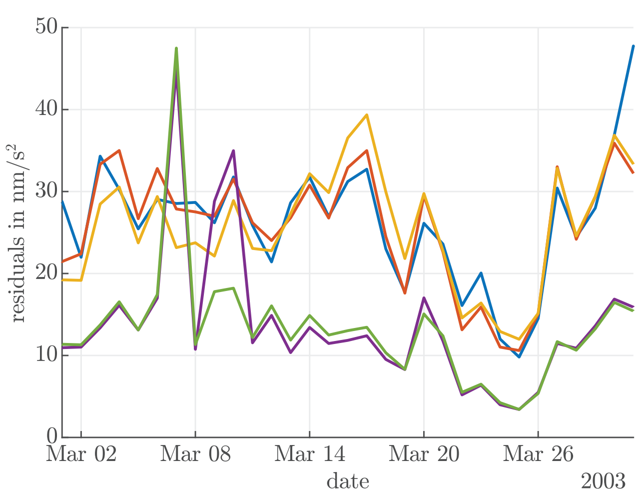

(a) March 2003

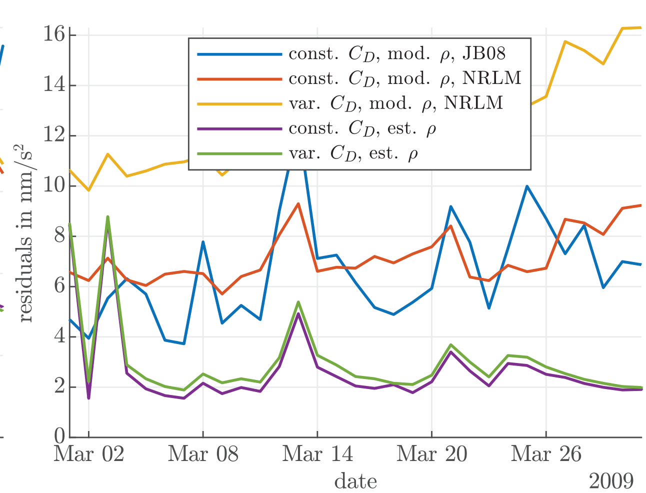

(b) March 2009

Fig. 21. Daily root mean square values of the differences in SRF x-axis of artificial acceleration data utilizing modelled and estimated density values with respect to daily-bias calibrated SDS ACC1B data for GRACE-B and March 2003 and March 2009.

missing for more than 10 days which would yield incomparable solutions. Additionally, one month in 2023 was processed to make a statement about the performance of our artificial acceleration and transplant data during higher solar activity periods. All solutions have been generated with GROOPS. The utilization of a single processing tool allows us to disregard the recommendation of the SDS to replace the $C_{2,0}$ and $C_{3,0}$ with SLR derived values (Loomis et al., 2020). Keeping these low degree coefficients in the solutions allows us to do a more complete comparison of the impact of the different transplant products on the estimated gravity fields. Additionally, the accelerometer calibration method utilized in the ITSG processing, has been identified to considerably improve the low degree coefficients (Klinger and Mayer-Gürr, 2016).

To decide which combination yields the best results, several comparisons have been made. First, annual mean solutions are calculated from the monthly solutions for each combination. The monthly solutions vary slightly for the different combinations over the months of 2019 and hence annual mean solutions make for an easier comparison. These annual solutions are compared in terms of degree difference to a 2019 mean field of the GOCO06s gravitational model, the post-fit residuals of the satellite-to-satellite tracking (SST) measurements and spatial equivalent water height (EWH) plots.

Fig. 22 shows the degree differences of seven mean 2019 solutions based on artificial data with respect to a mean 2019 GOCO06s field. For all three calibration variants, two estimation options are pictured. One for a constant C_D input and density estimation and one for a variable C_D input and $C_D\rho$ estimation. Solutions from var. C_D input and density estimation are not shown, as they have been identified as less performant in prior investigations. Apart from a mean 2019 ITSG solution also results with JPL and TUG transplants are computed with GROOPS and shown as references.

It can be seen that our transplant solutions agree with the ITSG really well up to degree 35. For higher degrees a divergence not only from the ITSG but also the JPL and TUG transplant references is visible. This shows a satisfactory performance of our minimalistic transplant approach compared to the complex transplants of JPL and TUG. The JPL transplants profits from information from the raw GRACE-D accelerometer data, which increases the quality for degrees higher than 35 (McCullough et al., 2022). Also the second degree difference of the JPL transplant is significantly lower than for any other data set. For the TUG transplant the better performance in the higher degrees can originate in the transplanted property. TUG estimates a vector property through incorporation of uniform cubic basis splines to account for temporal changes (Behzadpour et al., 2021). This vector reduces residuals for GRACE-D in all three axes opposed to the scalar aerodynamic property in our transplant, which aligns with studies conducted in Wöske (2021). There, it was shown that higher noise levels in x- and z-axis have a largely negative effect on gravity-field solutions, independent of each other. The impact in y-axis is not as large which justifies the mounting orientation of the accelerometer in GRACE-FO with the least sensitive axis in the SRF y-axis (Kornfeld et al., 2019). The solutions for the three different calibration options are very close together, as differences are nearly equalized by the variable acceleration calibration parametrisation in GROOPS. The same holds for the different density estimation parameters of our transplant. Fig. 22 also shows the impact in the

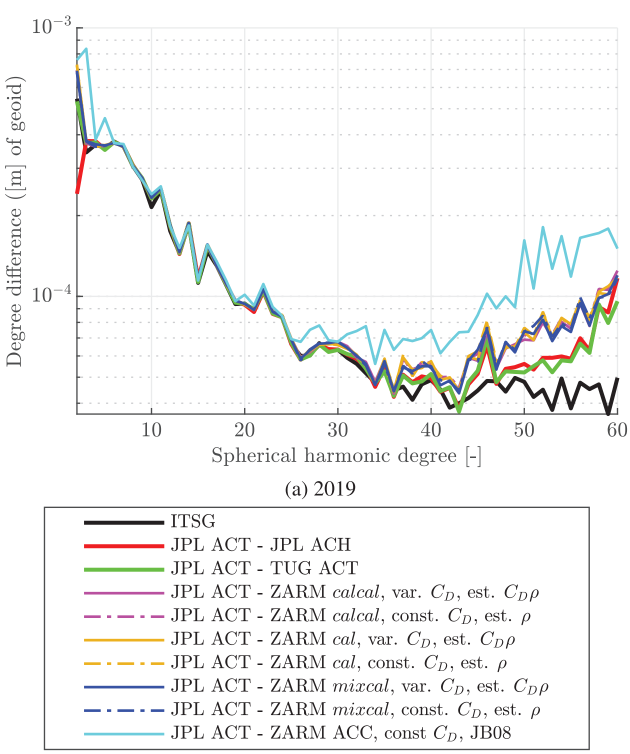

(a) 2019

(b) Legend

Fig. 22. Degree difference of annual mean gravity field solutions for 2019 with respect to the 2019 mean GOCO06s. Annual solutions for 2019 are calculated by averaging the monthly solutions.

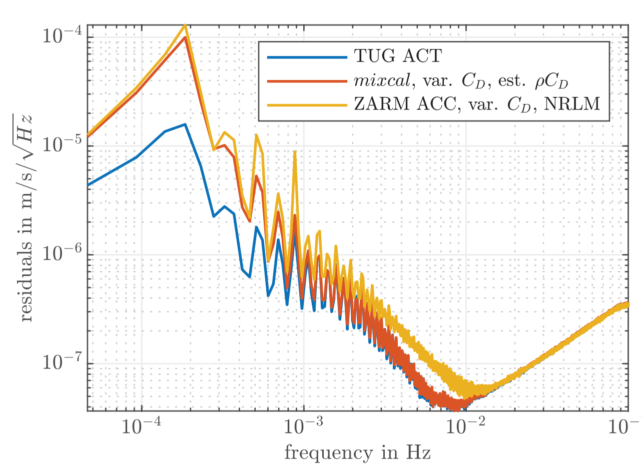

Fig. 23. SST ASD for the mean 2019 solution of ZARM artificial and transplant data. TUG transplant as reference.

higher degrees of the previously mentioned idiosyncrasies of the GROOPS GRACE example with respect to the ITSG operational setup (see Section 4).

Regarding the impact of our transplant procedure on the artificial acceleration data the blue graph for the ZARM ACC combination can be compared to any graph with transplant data for GRACE-D. Here, the largest impact of the transplant can be seen for the degrees three and five. The impact of our transplant on degrees two and four is surprisingly small. For degrees higher than 25 the quality is also significantly increased by utilizing transplanted data for GRACE-D in GFR.

In Fig. 23 the SST amplitude spectral density (ASD) of the SST residuals for three cases are pictured. As a reference the SST ASD of a solution utilizing the TUG transplant is given as well. The graphs for the ZARM data sets show the improvement of the solution due to utilization of transplant data. Up to a frequency of 10^{-2} Hz the transplant solutions continuously shows smaller residuals. Multiples of the orbital frequency are especially visible in the ASD plot, with the first maximum being the orbit frequency itself. For odd numbered multiples the improvement of the ZARM data is more prominent than for even numbered multiples. Regarding the TUG transplant, it can be seen that the residuals are noticeably lower up to a frequency of 10^{-3}. The difference to our transplant is largest for the orbit frequency and reduces with increasing frequency. This figure again shows the similarity of solutions with our and other transplants for certain frequency ranges and the diverging characteristics due to the different transplant strategies. The full transplant of TUG leads to smaller residuals for low frequencies and smaller degree difference for higher degrees (see Fig. 22).

The similarity of our transplant solutions to the transplants of JPL and TUG is also apparent as EWH plots with respect to a mean 2019 GOCO06s gravity field, which is pictured in Fig. 24. Only one transplant solution is presented due to the high similarity of the different transplant variations. The chosen solution is the *mixcal* calibration with variable C_D input and estimation of a combined density and drag coefficient. Overall, the pictured EWH plots show all the same signals. The differences of the solutions is most visible in the striping pattern, which is more prominent for our transplant. Additional differences can be identified in this plot only in the most prominent signals. Compare the EWH in India, southern Africa and South America.

For a comparison of the transplant variations, EWH plots of the other five transplant variation and the TUG transplant with respect to the *mixcal*, var. C_D, est. $C_D\rho$ have been computed. These six comparisons can be found in Fig. 25. The reference variation has been chosen as our best performing transplant compared to the TUG transplant. This means the other variations all show higher degree variances and EWH differences. The comparison in Fig. 25 show that the transplants with the same drag coefficient input and estimation factor agree better with the reference than the second input and estimation variation of the same calibration option. This comparison also shows that the *cal* calibration solutions differ the most and therefore are of the lowest quality. Overall, the transplant variations differ only in the higher degrees apparent

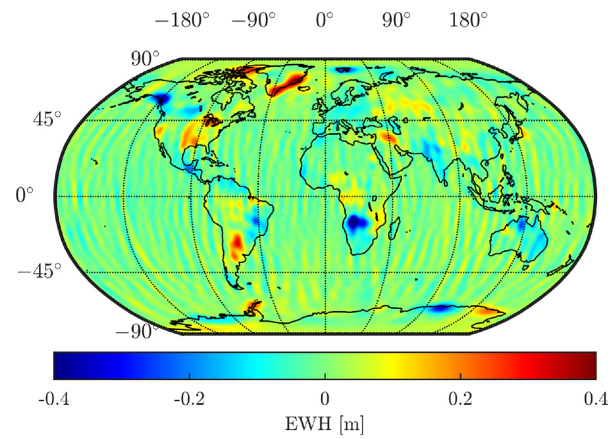

(a) *mixcal*, var. C_D, est. $C_D\rho$, rms = 5.349 cm

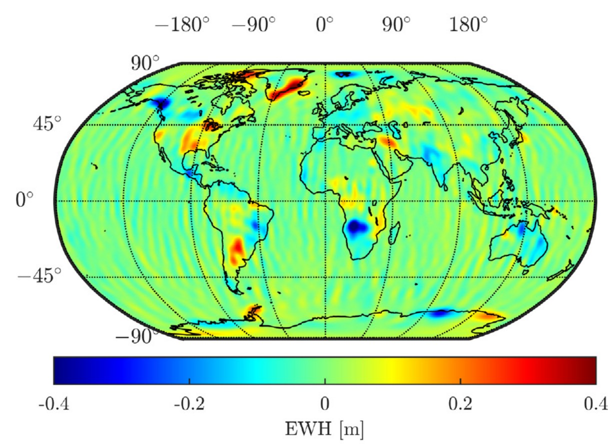

(b) TUG, rms = 5.01 cm

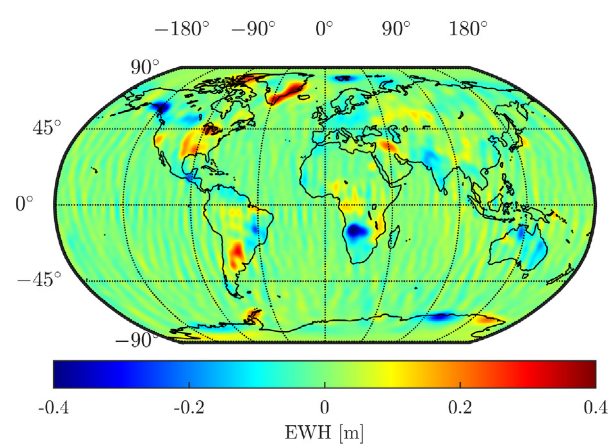

(c) JPL, rms = 5.006 cm

Fig. 24. Mean equivalent water height of various transplant data sets for 2019 with respect to mean 2019 GOCO06s. Gaussian-filter radius 200 km.

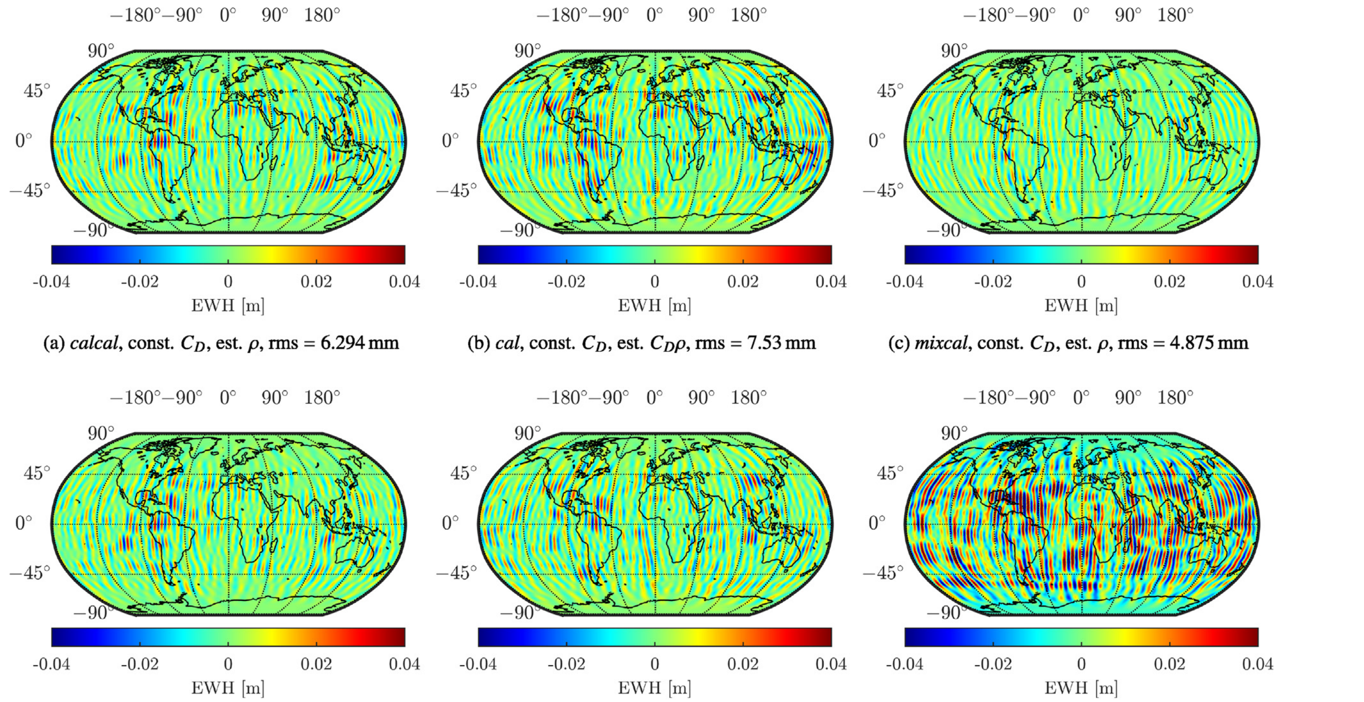

(a) *calcal*, const. C_D, est. ρ, rms = 6.294 mm (b) *cal*, const. C_D, est. $C_D\rho$, rms = 7.53 mm (c) *mixcal*, const. C_D, est. ρ, rms = 4.875 mm

(d) *calcal*, var. C_D, est. $C_D\rho$, rms = 6.149 mm (e) *cal*, var. C_D, est. $C_D\rho$, rms = 7.207 mm (f) TUG, rms = 13.859 mm

Fig. 25. Mean equivalent water height of various transplant data sets for 2019 with respect to *mixcal*, var. C_D, est. $C_D\rho$. Gaussian-filter radius 200 km.

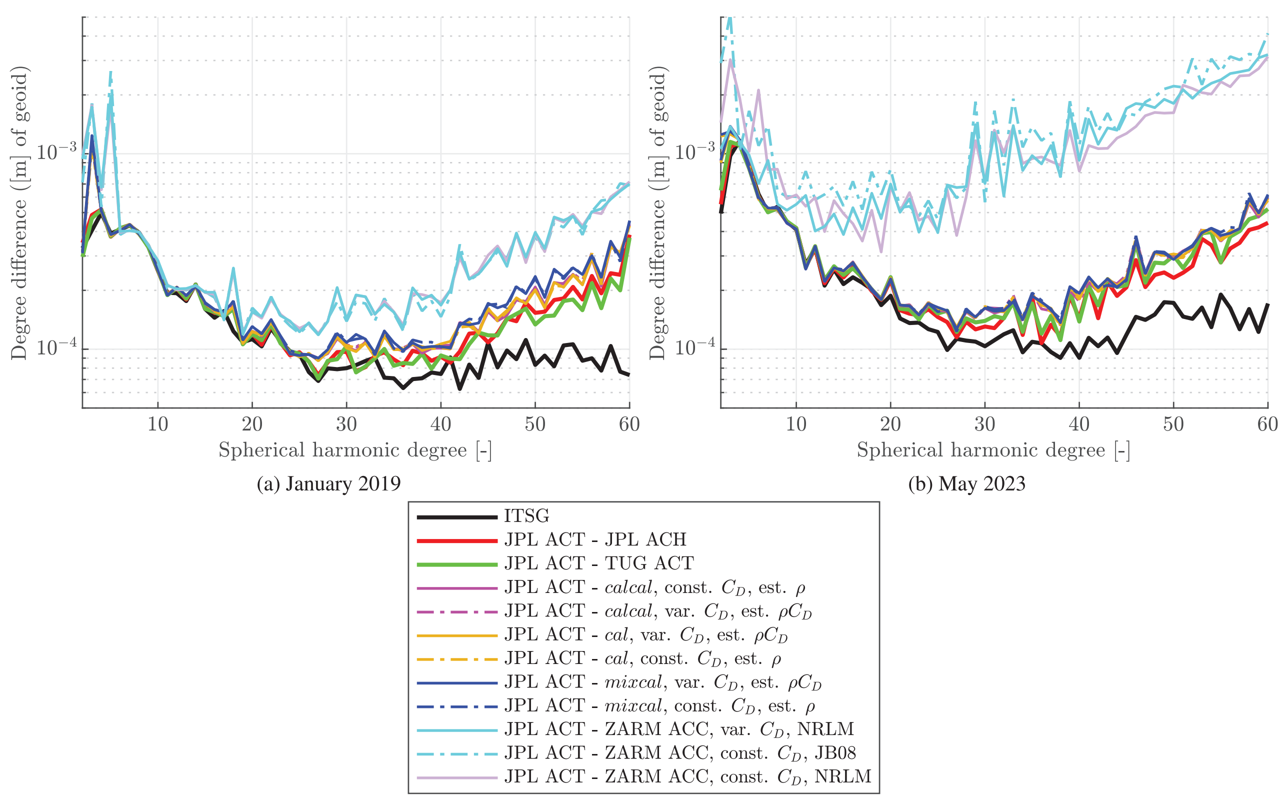

(a) January 2019 (b) May 2023

(c) Legend

Fig. 26. Degree difference of solutions for January 2019 and May 2023 with respect to a mean GOCO06s for the respective year.

due to a fine striping pattern and some dedicated differences at certain coordinates. By contrast, the comparison to TUG shows divergence also in lower degrees indicated by negative differences around the poles as well as more prominent and coarse striping.

Comparison of the performance of monthly solutions for dedicated months with low and high solar activity gives insight in the importance of the transplant for our artificial acceleration data. The solutions for January 2019 and May 2023 are presented in Fig. 26 in terms of degree differences. In January 2019 the solar activity is near a minimum and the atmospheric models describe the actual conditions well. In May 2023 the solar activity is significantly higher and the quality of the atmospheric models is reduced, as also shown through daily residuals in Fig. 8. This leads to a gravity field estimate with higher degree differences for May 2023 when utilizing artificial GRACE-D acceleration data (compare e.g. cyan graphs in Fig. 26). No solutions utilizing only artificial data are depicted as it was shown in Fig. 11 that the results vary insignificantly from combinations of real and modelled acceleration data. Therefore a reduction of quality can also be assumed for gravity field solutions with only artificial data for periods with higher solar activity.

The overall quality of all solutions, including the references of ITSG, JPL and TUG, is slightly decreased. The separation of the graphs for solutions with artificial data and transplants indicate the increased importance of the transplant procedure for higher solar activity. In May 2023 our transplant variations not only perform better in terms of lower degree difference compared to artificial data but also compared to the transplants of JPL and TUG. The separation to JPL and TUG transplant solutions is smaller for May 2023, yielding solutions of comparable quality over all degrees.

The May 2023 solutions also show increased differences between the ZARM ACC solutions. The solution with variable C_D and NRLMSISE-00 shows lower residuals for the first 15 degrees, for higher degrees it varies which of the three combinations yield the lowest degree differences. This months suggest that the variable C_D model and an incorporation of a dedicated lift calculation performs better for periods with higher solar activity. Additionally, the NRLMSISE-00 model seems to perform better in the higher degrees than the JB08 model.

8. Conclusion

We described the development of an alternative transplant procedure that generates acceleration data for the GRACE-D satellite as independent as possible from GRACE-C data. For this we used a high-precision environment modelling approach (see Section 3).

We showed that the atmospheric models supplying values for the thermospheric density are a limiting factor due to their high uncertainties in combination with the correct estimation of the drag coefficient C_D. These models limit the data quality especially in the along-track direction which is also the main measurement direction of the GRACE-FO mission, thus directly coupling into the GFR performance. Gravity field solutions have been generated with combinations of real and artificial data to study the potential of the high-precision environment modelling in geodesy applications. We are able to generate gravity field solutions with a combination of real and artificial or only artificial data, but are limited in terms of quality by the uncertainties of the atmospheric drag modelling. For periods with higher solar activity, the quality of the estimated gravity fields decreases due to increasing uncertainties in the atmospheric models. In principle, gravity field solutions can be generated for satellite missions without on-board accelerometer based on high-precision environment modelling. It has to be emphasised that these solutions would be a lot more restricted by the atmospheric model than the GRACE-FO solutions investigated here. For GRACE-FO, it was shown that combinations of real accelerometer data for GRACE-C and artificial data for GRACE-D could not compete with solutions using transplant data from TUG or JPL for the second satellite (see Section 4), due to the drag acceleration. For higher orbits with less atmospheric influence, our artificial acceleration data would perform better due to the precise radiation models. These findings motivate the development of our transplant procedure that aims to generate accelerometer data for GRACE-D with as little dependency on GRACE-C data as possible (see Section 5). This is done opposed to transplants from JPL, who transplant the whole accelerometer product and apply corrections based on GRACE-D raw acceleration data. Or the transplant from TUG, who estimate correction factors for all three axes of the GRACE-C accelerometer and transplant this vector to GRACE-D.

Our transplant procedure is based on the estimation of thermospheric density values that better describe the atmospheric state at the satellite's position than the atmosphere models. Estimated values are then used to calculate the atmospheric perturbations acting on GRACE-D.

The validation of our transplant data showed that the estimated density significantly reduces the residuals in the along-track axis for both satellites. The reduction of the residuals is slightly smaller for GRACE-D but still yields an improvement of the data of approximately one order of magnitude (see Fig. 15).

Gravity field solutions generated with our in–house GFR tool allows us to investigate the complete process chain and study various influences in data generation and gravity field determination procedures. However, the quality of gravity field solutions from our in–house tool is inferior compared to solutions generated with tools from other processing centres. Therefore, the GROOPS tool of TUG is used for the presented gravity field solutions. The conducted studies showed several valuable properties of our artificial and transplant data and the transplant procedure.

The increased quality of the artificial acceleration by the transplant procedure directly translates into the gravity field solutions. Utilizing our transplant data enabled us to estimate gravity fields closely comparable to solutions using transplant data from JPL or TUG. This validates our aim to develop a minimalistic and physically motivated transplant procedure. It is also shown that the gain in quality through the transplant procedure increases with increasing solar activity (see Fig. 26). The different in–house transplant variations showed only little differences among themselves in 2019. For the single processed month of 2023 this circumstance does not change, showing that the transplant procedure performs at the same level for higher solar activity. The 2023 solution also shows a slightly better agreement to other transplants. However, to be able to asses the performance during high solar activity periods more months have to be processed.

Comparisons of gravity field solutions with our in–house tool, GROOPS and utilizing different transplant products enabled us to identify improvement possibilities in both our gravity-field recovery tool and the transplant procedure. But also possibilities to improve the high-precision environment modelling have been identified. Investigation of the residuals in the three satellite reference frame axes (e.g. see Fig. 18), revealed patterns that can be ascribed to radiation perturbations and reflections from satellite parts onto other. The incorporation of a ray-tracing algorithm for the radiation perturbations is the next development step for this finding.

The ZARM transplant product is published alongside a radiation acceleration and estimated density product as complementary data to this paper and publicly available at: https://www.zarm.uni-bremen.de/zarm_daten/.

Declaration of Competing Interest

The authors declare that they have no known competing financial interests or personal relationships that could have appeared to influence the work reported in this paper.

Acknowledgments

This work is part of the Collaborative Research Center 1464 TerraQ and funded by Deutsche Forschungsgemeinschaft DFG.

The contributions of F. Wöske and B. Rievers have been supported by the Federal Ministry for Economic Affairs and Climate Action via the German Aerospace Center (DLR) within the project GRACEAERO/SD FKZ 50LZ 2101 and DEOS-AERO 50LZ2302.

We thank F. Öhlinger and T. Mayer-Gürr for the valuable discussions and the data exchange.

References

Bandikova, T., McCullough, C., Kruizinga, G.L., et al., 2019. GRACE accelerometer data transplant. Adv. Space Res. 64 (3), 623–644. https://doi.org/10.1016/j.asr.2019.05.021.

Behzadpour, S., Mayer-Gürr, T., Flury, J., et al., 2019. Multiresolution wavelet analysis applied to GRACE range-rate residuals. Geoscient. Instrum., Methods Data Syst. 8 (2), 197–207. https://doi.org/10.5194/gi-8-197-2019.

Behzadpour, S., Mayer-Gürr, T., Krauss, S., 2021. GRACE follow-on accelerometer data recovery. J. Geophys. Res.: Solid Earth 126 (5). https://doi.org/10.1029/2020JB021297.

Bowman, B., Tobiska, W.K., Marcos, F., et al., 2008. A New Empirical Thermospheric Density Model JB2008 Using New Solar and Geomagnetic Indices. In: AIAA/AAS Astrodynamics Specialist Conference and Exhibit. American Institute of Aeronautics and Astronautics, Honolulu, Hawaii. https://doi.org/10.2514/6.2008-6438.

Bruinsma, S., 2015. The DTM-2013 thermosphere model. J. Space Weather Space Climate 5, A1. https://doi.org/10.1051/swsc/2015001.

Christophe, B., Boulanger, D., Foulon, B., et al., 2015. A new generation of ultra-sensitive electrostatic accelerometers for GRACE Follow-on and towards the next generation gravity missions. Acta Astronaut. 117, 1–7. https://doi.org/10.1016/j.actaastro.2015.06.021.

Dill, R., 2008. Hydrological model LSDM for operational Earth rotation and gravity field variations. https://doi.org/10.2312/GFZ.b103-08095.

Doornbos, E., 2011. Thermospheric Density and Wind Determination from Satellite Dynamics. Springer, Berlin Heidelberg Berlin, Heidelberg. https://doi.org/10.1007/978-3-642-25129-0, Ph.D. thesis.

Drob, D.P., Emmert, J.T., Meriwether, J.W., et al., 2015. An update to the Horizontal Wind Model (HWM): The quiet time thermosphere. Earth Space Sci. 2 (7), 301–319. https://doi.org/10.1002/2014EA000089.

Harvey, N., McCullough, C.M., Save, H., 2022. Modeling GRACE-FO accelerometer data for the version 04 release. Adv. Space Res. 69 (3), 1393–1407. https://doi.org/10.1016/j.asr.2021.10.056.

JPL (2023). Technical Note 01a, Spacecraft Events log. Technical Note TN-01a_SCE Jet Propulsion Laboratory, California Institute of Technology.

Klinger, B., Mayer-Gürr, T., 2016. The role of accelerometer data calibration within GRACE gravity field recovery: Results from ITSG-Grace2016. Adv. Space Res. 58 (9), 1597–1609. https://doi.org/10.1016/j.asr.2016.08.007.

Kornfeld, R.P., Arnold, B.W., Gross, M.A., et al., 2019. GRACE-FO: The Gravity Recovery and Climate Experiment Follow-On Mission. Journal of Spacecraft and Rockets 56 (3), 931–951. https://doi.org/10.2514/1.A34326.

Kvas, A., Behzadpour, S., Ellmer, M., et al., 2019. ITSG-Grace2018: Overview and Evaluation of a New GRACE-Only Gravity Field Time Series. J. Geophys. Res.: Solid Earth 124 (8), 9332–9344. https://doi.org/10.1029/2019JB017415.

Kvas, A., Brockmann, J.M., Krauss, S., et al., 2021. GOCO06s – a satellite-only global gravity field model. Earth System Science Data 13 (1), 99–118. https://doi.org/10.5194/essd-13-99-2021.

Kvas, A., Mayer-Gürr, T., 2019. GRACE gravity field recovery with background model uncertainties. J. Geodesy 93 (12), 2543–2552. https://doi.org/10.1007/s00190-019-01314-1.

Landerer, F.W., Flechtner, F.M., Save, H., et al., 2020. Extending the Global Mass Change Data Record: GRACE Follow-On Instrument and Science Data Performance. Geophys. Res. Lett. 47 (12). https://doi.org/10.1029/2020GL088306, e2020GL088306.

Loomis, B.D., Rachlin, K.E., Wiese, D.N., et al., 2020. Replacing GRACE/GRACE-FO With Satellite Laser Ranging: Impacts on Antarctic Ice Sheet Mass Change. Geophys. Res. Lett. 47 (3). https://doi.org/10.1029/2019GL085488, e2019GL085488.

Mayer-Gürr, T., Behzadpour, S., Eicker, A., et al., 2021. GROOPS: A software toolkit for gravity field recovery and GNSS processing. Comput. Geosci. 155, 104864. https://doi.org/10.1016/j.cageo.2021.104864.

McCullough, C., Harvey, N., Save, H., et al., 2022. Operational GRACE-FO Accelerometer Transplant Strategies. AGU Fall Meeting, Chicago, USA.

NASA Jet Propulsion Laboratory (JPL) (2019). GRACE-FO Level-1B Release version 4.0 from JPL in ASCII. doi:10.5067/GFL1B-ASJ04.

Öhlinger, F.L. (2023). GRACE cookbook differences to ITSG processing, personal correspondance.

Picone, J.M., Hedin, A.E., Drob, D.P., et al., 2002. NRLMSISE-00 empirical model of the atmosphere: Statistical comparisons and scientific issues: TECHNIQUES. J. Geophys. Res.: Space Phys. 107 (A12), SIA 15-1–SIA 15-16. https://doi.org/10.1029/2002JA009430.

Prussing, J.E., Conway, B.A., 1993. Orbital mechanics. Oxford University Press, New York.

Robertson, R.V. (2015). Highly Physical Solar Radiation Pressure Modeling During Penumbra Transitions. Dissertation Virginia Polytechnic Institute and State University. URL: https://www.proquest.com/dissertations-theses/highly-physical-solar-radiation-pressure-modeling/docview/1942886437/se-2.

Sentman, H. (1961). Free molecule flow theory and its application to the determination of aerodynamic forces. URL: https://api.semanticscholar.org/CorpusID:92321666.

Tapley, B.D., Bettadpur, S., Watkins, M., et al., 2004. The gravity recovery and climate experiment: Mission overview and early results. Geophys. Res. Lett. 31 (9). https://doi.org/10.1029/2004GL019920, 2004GL019920.

Webb, F.H., Flechtner, F.M., Landerer, F., et al., 2019. Science Data System Newsletter Report, June 2019 (No. 4). URL: https://media.gfz-potsdam.de/gfz/sec12/pdf/GRACE_FO_SDS_newsletter_No4.pdf.

Wen, H.Y., Kruizinga, G., Paik, M., et al., 2019. Gravity Recovery and Climate Experiment Follow-On (GRACE-FO) Level-1 Data Product User Handbook. Technical Report Jet Propulsion Laboratory, California Institute of Technology, URL: https://archive.podaac.earthdata.nasa.gov/podaac-ops-cumulus-docs/gracefo/open/docs/GRACE-FO_L1_Handbook.pdf.

Wöske, F., 2021. Gravity Field Recovery from GRACE Satellite Data and Investigation of Sensor. Environment and Processing-Option Influences by Closed Loop Mission Simulation. https://doi.org/10.26092/elib/1384.

Wöske, F., Kato, T., Rievers, B., et al., 2019. GRACE accelerometer calibration by high precision non-gravitational force modeling. Adv. Space Res. 63 (3), 1318–1335. https://doi.org/10.1016/j.asr.2018.10.025.

Wöske, F., Rievers, B., 2022. Thermospheric Density Estimation from Accelerometer Data of Geodetic Satellites – Evaluation of Sensitivity towards Non-Gravitational Force Modeling, POD calibration, and Comparison of Results. In: AGU Fall Meeting, SA45C-2177. Sanfrancisco, USA.

Wöske, F., Rievers, B., 2023. ZARM thermospheric neutral density solution from GRACE accelerometer data: Approach, validation and comparison. In: EGU General Assembly, EGU23-12476. Wien, Austria. https://doi.org/10.5194/egusphere-egu23-12476.

Wu, S.-C., Kruizinga, G., Bertiger, W., 2006. Algorithm Theoretical Basis Document for GRACE Level-1B Data Processing V1.2. California Institute of Technology, Technical Report Jet Propulsion Laboratory, URL: https://archive.podaac.earthdata.nasa.gov/podaac-ops-cumulus-docs/grace/open/docs/ATBD_L1B_v1.2.pdf..